https://doi.org/10.5194/essd-2025-384
Preprint. Discussion started: 10 July 2025

Open Access Earth System Science Data Discussions

A Black Hole Eddy Dataset of North Pacific Ocean Based on Satellite Altimetry

Fenglin Tian[1, 2, 3, *], Yingying Zhao[1], Lan Qin[1], Shuang Long[1], Ge Chen[1, 2, 3]

[1] College of Marine Technology, Faculty of Information Science and Engineering, Ocean University of China, Qingdao, 266100, China
[2] Frontiers Science Center for Deep Ocean Multispheres and Earth System, Ocean University of China, Qingdao, 266100, China
[3] Laoshan Laboratory, Qingdao, 266237, China

Correspondence to: Fenglin Tian (tianfenglin@ouc.edu.cn)

Abstract. The methodologies employed for the identification of ocean coherent eddies can be categorized as either Eulerian and Lagrangian. Among Lagrangian structures, Black Hole Eddies (BHEs) exhibit the highest degree of material coherence and conservation, making them particularly suitable for studying the transport and retention of oceanic materials. This study presents an efficient Graphics Processing Unit (GPU) -based BHE identification algorithm, enhancing computational efficiency by approximately 13 times compared to the existing methods. Using this algorithm, the North Pacific Black Hole Eddy dataset (BHE v1.0) is constructed for the first time, based on satellite-derived surface geostrophic velocity data from January 1, 1993 to May 5, 2023 (Tian, F. L., Zhao, Y. Y., Long, S., and Chen, G.: A Black Hole Eddy Dataset of North Pacific Ocean Based on Satellite Altimetry (BHE v1.0). Zenodo [data set], https://doi.org/10.5281/zenodo.15597447, 2025a.. BHE v1.0 contains 18387 eddies with radius larger than 20 km and lifetimes longer than 4 weeks and captures both the spatial-temporal characteristics and the trajectories of coherent eddies throughout lifetimes. Through the advection of Lagrangian particles in Eulerian eddy, rotationally coherent Lagrangian vortices (RCLVs) and BHEs, it is confirmed that BHEs maintain strong material coherence and are able to maintain concentration during their life cycle, preserving their structure without significant filamentation or mixing with surrounding waters. Additionally, approximately 6% of BHEs, which do not overlap with any RCLVs or Eulerian eddies, are identified and referred to as the Naked Black Hole Eddy and further analyze its coherence through advection. And Transport analysis shows that BHEs induce westward transport about 1.5 Sv, three times weaker than RCLVs, suggesting that they may offer a more accurate estimate of oceanic transport than RCLVs. These finding addresses the existing gap in Black Hole Eddy datasets within the field of oceanography and provides a novel perspective for studying the interactions between coherent eddies and oceanic physical phenomena.

1 Introduction

Mesoscale eddies, one of the most prominent processes in the ocean, typically range from several tens to hundreds of kilometers in spatial scale and can persist for periods of a few weeks to several years (Chelton et al., 2011a; Chaigneau et al.,

https://doi.org/10.5194/essd-2025-384
Preprint. Discussion started: 10 July 2025

2008). Mesoscale eddies are ubiquitous in the ocean and play a crucial role in the transport of heat, salinity, and other various variables, further influencing on the marine material cycle, large-scale water body transport, and biological activities (Chen et al., 2012; Chen et al., 2021; Faghmous et al., 2015; Dong et al., 2014). In recent years, mesoscale eddies have become a major focus of research within the field of oceanography(Chelton et al., 2011b).

Existing mesoscale eddy identification algorithms are primarily categorized into Eulerian and Lagrangian methods. The Eulerian approachs are based on the instantaneous state of the flow field and relies on a fixed reference coordinate system (Serra and Haller, 2016), which can be categorized into three major categories: (1) extraction methods that utilize physical parameters, including the Okubo-Weiss (OW) parameter method (Chelton et al., 2007; Henson and Thomas, 2008), and the Winding-Angle (WA) method (Chaigneau et al., 2008; Sadarjoen and Post, 2000); (2) extraction methods that are based on the direction of ocean currents (Nencioli et al., 2010; Williams et al., 2011); and (3) extraction methods based on sea surface height (SSH) (Chelton et al., 2011b; Faghmous et al., 2015; Mason et al., 2014). However, the Eulerian methods have several limitations. On the one hand, they are frame-dependent, while the flow field in the real ocean does not have a fixed reference frame, which may cause the results to lose coherence under coordinate transformation. On the other hand, due to the transient characteristics of the fluid, a body of water within the Eulerian boundary can generate numerous filaments and disperse rapidly, potentially resulting in an overestimation of the eddy's transport capacity.

The Lagrangian methods are proposed based on the accumulation of fluid states within a flow field over a specified duration (Haller, 2015). In contrast to the Eulerian approachs, the Lagrangian methods conceptualize eddies as coherent structures within the oceanic environment. Due to the boundaries' ability to maintain stability over a finite time (Provenzale, 1999), Lagrangian eddies are demonstrated to exhibit material coherence. Therefore, Lagrangian eddies provide a more accurate structures of oceanic mesoscale eddies, particularly within unstable flow fields. Furthermore, Lagrangian eddies are effective in quantifying the material transport capacity of these eddies (Tian et al., 2019; Tian et al., 2022).

Before Lagrangian coherent structures (LCSs) entered into strict mathematical definitions, heuristic criteria methods such as the Finite-Time Lyapunov Exponent (FTLE) (Shadden et al., 2005; Haller, 2011) and the Finite-Size Lyapunov Exponent (FSLE) (D'ovidio et al., 2004; Joseph and Legras, 2002; Aurell et al., 1997) have been proposed to identify coherent structure. But these heuristic methods lack material invariance, depend sensitively on thresholds and resolution, and are inadequate for capturing coherent structures in chaotic or finite-time dynamical systems (Beron-Vera et al., 2010; Beron-Vera et al., 2012; Haller, 2015; Peacock and Haller, 2013; Onu et al., 2015). To address these limitations, Haller and Beron-Vera (2012) introduced a geodesic framework in which elliptic LCSs are defined as closed material curves that minimize stretching, corresponding to closed geodesics of a Riemannian metric derived from the flow’s Cauchy-Green strain tensor. Subsequently, Haller and Beron-Vera (2013) introduced a rigorous variational framework for detecting coherent Lagrangian vortices. These vortices are defined as closed material curves that exhibit minimal stretching and filamentation throughout their evolution, providing an objective basis for identifying coherent structures in unsteady flows. These eddies boundary are commonly referred to as the "photon sphere, analogous to Black Holes found in the universe". Once matter crosses this boundary, it becomes trapped within the eddy, there giving rise to the term Black Hole Eddy (BHE). Building on this

https://doi.org/10.5194/essd-2025-384
Preprint. Discussion started: 10 July 2025

theoretical foundation, Karrasch et al. (2015) developed an automated numerical algorithm that detects such vortex boundaries by computing the Cauchy-Green strain tensor from the flow map and extracting closed tensorlines aligned with its eigenvector fields. This approach enables the systematic and frame-independent identification of elliptic LCSs, facilitating practical analysis of coherent vortices in real oceanic flows. Later, Serra and Haller (2017) presented a simplified and efficient algorithm for computing closed null geodesics that define coherent vortex boundaries in two-dimensional flows, enabling fully automated and robust BHE boundary detection. Using the extraction method of BHE, Beron-Vera et al. (2013) extracted and analyzed the boundaries of the Agulhas eddy, the body of water enveloped by the Lagrangian eddy can continuously maintain independent rotation, and provided a coherent description of its boundary changes. Haller et al. (2018) subsequently introduced the automatically extracted eddy boundary into all randomly diffusing flow fields, considering this eddy boundary as a material barrier for diffusion and random transport. This approach demonstrates greater efficiency compared to previous Lagrangian eddy identification methods and enhances the objectivity of eddy boundary identification. Therefore, the process of solving BHE is complex (Karrasch and Schilling, 2020), but they still maintain superior coherence in the long-term transportation of flow fields. But due to the inherent complexity of the algorithm designed for detecting BHE, an efficient detection algorithm for such eddies has yet to be developed.

Compared to Lagrangian approaches, Eulerian eddy datasets were developed earlier on a global scale due to the relative simplicity of their detection methods. In recent years, the number of published Eulerian eddy datasets has grown significantly, driven by the increasing availability of satellite altimeter products and the growing interest in mesoscale ocean dynamics. Using 16 years of SSH data constructed by merging the measurements from two simultaneously operating altimeters, Chelton et al. (2011b) employed the closed contour method to generate the first global eddy dataset and analyze the general features of mesoscale eddies. Mason et al. (2014) proposed an open-source mesoscale eddy identification and automatic tracking algorithm, known as py-eddy-tracker (PET). Based on sea level anomaly (SLA), PET effectively tracks eddy trajectories within user-defined regions. The method introduces key innovations by utilizing interpolated SLA contours, incorporating rigorous shape tests, and applying a speed-based criterion to define eddy boundaries and centers, thereby enhancing tracking accuracy and consistency compared to CSS11. Later, based on the most recent version of postprocessed daily SLA estimates that better resolves mesoscale features than the version used by CSS11, Faghmous et al. (2015) presented a global daily mesoscale ocean eddy dataset that contains ~45 million mesoscale eddies and 3.3 million eddy trajectories. Based on CSS11 code, the global Mesoscale Eddy Trajectory Atlases (META 2.0) was produced by SSALTO/DUACS and distributed by Archiving, Validation and Interpretation of Satellite Oceanographic (AVISO), with support from the National Centre for Space Studies, in collaboration with Oregon State University and support from the National Aeronautics and Space Administration. Furthermore, Tian et al. (2020) developed a parallelized identification and tracking framework for global mesoscale eddies based on merged multi-satellite altimeter data. The approach employs refined contour-based boundary extraction and introduces a synthetic "fake eddy" mechanism to accommodate short-term surface signal loss, thereby enhancing the temporal continuity and robustness of eddy trajectories. In order to better represent the dynamics in the more energetic oceanic regions and in the vicinity of coasts and islands, based on the absolute dynamic

https://doi.org/10.5194/essd-2025-384
Preprint. Discussion started: 10 July 2025

topography (ADT) field, instead of the previous SLA maps, Pegliasco et al. (2022) presented META3.1exp, which consists of eddy identifications and trajectories derived from altimetric maps. The detection methodology utilized is based on the PET algorithm developed by Mason et al. (2014).

In contrast to the earlier development of Eulerian eddy datasets, the advancement of Lagrangian eddy datasets has been relatively limited due to methodological and computational challenges. Tian et al. (2022) employed the orthogonal parallel architecture algorithm to identify and release a global Lagrangian eddy dataset, achieving a significant enhancement in identification efficiency, with a computational speed increase of up to 500 times, and using advection particles found that lagrangian eddies have better material coherence and objectivity than Eulerian eddies. Later, Liu and Abernathey (2023) employed the Lagrangian-averaged vorticity deviation (LAVD) method to generate a global Lagrangian eddy dataset GLED v1.0 based on altimetry observations. This dataset not only delineates the general characteristics of eddies with T=30-day and 90-day, such as the position of the eddy center, equivalent radius, and rotational properties, but also includes the particle trajectories delineated by the coherent eddy boundaries throughout their entire life cycle. Utilizing the LAVD method, Xia et al. (2022) detected nine long-lived Agulhas rings and categorized their life cycles into two distinct stages: growth and extinction, which introduced the concept of a material belt and investigated the factors contributing to the longevity of Agulhas rings by establishing a linear relationship between the average strain rate and the square root of kinetic energy. To elucidate biogeochemical developments within eddies, Jones-Kellett and Follows (2024) used a backward-in-time Lagrangian particle tracking approach to identify rotationally coherent Lagrangian vortices (RCLVs) with a 32-day integration window and 8-day reinitialization intervals. Each vortex was tracked across its lifespan by following the trajectory of its core particle and linking coherent boundaries across consecutive time steps. This method highlights the material retention capacity of Lagrangian eddies, aligning more closely with biogeochemical responses that depend on the water mass. Despite the increasing comprehensiveness of eddy datasets, the majority are constructed under an Eulerian framework. In contrast, the Lagrangian framework faces challenges such as algorithmic complexity, low computational efficiency, resulting in a scarcity of global datasets pertaining to Lagrangian eddies. Furthermore, there is a notable lack of long-term Lagrangian datasets for specific marine regions, with most being primarily identified through the LAVD method. Consequently, long-term, and large-scale dataset products concerning BHE remain absent. Due to the lack of global or regional BHE data products, there remains a lack of analytical research on the material coherence, formation reasons, longevity, energy, and other characteristics.

Besides, previous studies found that fewer and smaller structures maintain coherency for longer timescales (Abernathey and Haller, 2018; Jones-Kellett and Follows, 2024; Xia et al., 2022; Liu and Abernathey, 2023). However, Jones-Kellett and Follows (2024) compared the atlas of Lagrangian coherent eddies with an atlas of Eulerian eddies and find that RCLVs may not overlap with Eulerian eddies. Consequently, it is unclear that whether the BHE is wrapped by the RCLVs and the Eulerian Eddies. Furthermore, does the RCLVs and Eulerian identification method fail to identify some coherent vortices? Comparing BHE dataset to RCLVs and Eulerian eddy atlases can answer these questions, revealing how the coherent properties of mesoscale features manifest in space and time.

https://doi.org/10.5194/essd-2025-384
Preprint. Discussion started: 10 July 2025

This study presents an efficient GPU-accelerated identification algorithm designed to enhance the geodesic algorithm proposed by Serra and Haller (2017) for identifying BHE. This advancement represents a significant improvement, achieving speeds that are 13 times faster than the original algorithm in the Lagrangian approach to Black Hole Eddy identification. Utilizing this efficient GPU-accelerated identification algorithm, a dataset of Black Hole Eddy in the North Pacific (0-50°N, 130°-270°E) is constructed for the first time spanning from January 1, 1993 to May 5, 2023, which addresses a notable gap in oceanography, as such a dataset previously did not exist. The North Pacific is selected as the study region due to its high eddy activity (Chelton et al., 2011b), extensive altimetric coverage favorable for coherent eddy detection (Chaigneau et al., 2008), and the crucial role of mesoscale eddies in modulating regional oceanic heat transport and biogeochemical dynamics (Qiu and Chen, 2005). Based on this dataset, we compare the Eulerian eddies and RCLVs to analyze the strong coherence of BHE and find the Naked Black Hole Eddy which neither overlap with Eulerian eddies nor with RCLVs. Additionally, we provide fundamental characteristics of BHE, including their lifespan, size, and geographic distribution. This represents first comprehensive analysis of BHE.

The organization of this article is structured as follows: Section 2 introduces the methodology for generating the North Pacific Black Hole Eddy dataset. Section 3 presents essential information about the dataset, including the statistical characteristics of the BHE, as well as comparisons with Eulerian eddies and RCLVs. Section 4 discusses the usability of the eddy dataset. Finally, Section 5 offers a summary and conclusion.

2 Data and methods

2.1 Data

2.1.1 Satellite altimetry data

This study utilizes the global gridded ADT data published by the Copernicus Marine Environment Monitoring Service (CMEMS). The ADT was determined through optimal interpolation, leveraging measurements from various altimeter missions at the Level 3 stage. This partially processed data has global applicability and provides additional variables, including ADT and both absolute and anomalous geostrophic currents. The ADT data included in this dataset were employed in our study. Processed by DUACS multi-mission altimeter data processing system, the data is intended for near-real-time applications. The spatial resolution of the data is 0.25° × 0.25°, and it offers a temporal resolution of one day. The dataset is publicly available at: https://data.marine.copernicus.eu/product/SEALEVEL_GLO_PHY_L4_NRT_008_046/description.

2.1.2 Chlorophyll *a* data

Chlorophyll *a* (Chla) data from the Ocean Colour Climate Change Initiative (OC_CCI, Ocean Colour Climate Change Initiative) project of the European Space Agency (ESA) is designed to provide high-quality long-term ocean water color data

https://doi.org/10.5194/essd-2025-384
Preprint. Discussion started: 10 July 2025

products for climate change studies fusing data from multiple satellite sensors, such as SeaWiFS, MODIS and MERIS, through band-shifting and bias-correction techniques, and using global measured data for error correction. It includes daily-averaged, 5-day-averaged, 8-day-averaged and monthly-averaged datasets with a spatial resolution of 0.25° × 0.25°and a time series covering from September 1997 to the present. The temporal resolution chosen for this paper is 1-day, and the data can be downloaded at: https://www.pml.ac.uk/science/Earth-Observation-Science-and-Applications.

2.1.3 Sea surface temperature data

Sea surface temperature (SST) data used in this study are obtained from the National Oceanic and Atmospheric Administration (NOAA) Physical Sciences Laboratory (PSL), specifically from the NOAA Optimum Interpolation Sea Surface Temperature version 2 (NOAA OISST v2) dataset. This product is generated by blending satellite observations (e.g., AVHRR), ship-based measurements, and buoy data using optimal interpolation techniques. The anomaly fields are calculated relative to a long-term climatology, and reflect deviations in SST associated with phenomena such as eddies, El Niño events, or seasonal variability. The data are provided in NetCDF format, with a global spatial resolution of 0.25° × 0.25° and temporal resolution of daily. The dataset can be accessed and downloaded from the NOAA PSL website: https://www.psl.noaa.gov/data/gridded/data.noaa.oisst.v2.highres.html.

2.1.4 Sea surface salinity data

Sea surface salinity (SSS) data used in this study are derived from the Global Ocean Ensemble Physics Reanalysis product (GLOBAL_MULTIYEAR_PHY_ENS_001_031), provided by the CMEMS. This ensemble reanalysis product offers global gridded estimates of key ocean physical variables, including temperature, salinity, ocean currents, and ice parameters, with a spatial resolution of 0.25° × 0.25°. The dataset spans from January 1, 1993 to December 31, 2023, and provides both daily and monthly averages over 75 vertical depth levels.This product is constructed by combining four different global ocean reanalysis systems: GLORYS2V4 (Mercator Ocean, France), ORAS5 (ECMWF), GloSea5 (UK Met Office), and C-GLORSv7 (CMCC, Italy). Each of these models assimilates satellite altimetry and in situ observations to reconstruct the ocean's physical state. The ensemble approach helps to quantify uncertainty and provide more robust estimates than individual reanalysis products. The data are accessible via CMEMS at: https://data.marine.copernicus.eu/product/GLOBAL_MULTIYEAR_PHY_ENS_001_031/description.

2.1.5 Mesoscale eddy data

The mesoscale Eulerian eddy dataset used in this study is the META3.1exp product developed by Pegliasco et al. (2022). META3.1exp provides a comprehensive catalog of mesoscale eddies, including their geographic locations, lifetime, propagation paths, amplitude, radius, polarity (cyclonic or anticyclonic), and other physical characteristics. The eddies are identified and tracked from gridded ADT fields derived from satellite altimetry maps distributed by AVISO (Archiving, Validation and Interpretation of Satellite Oceanographic data). The dataset covers the global ocean between 1993 and 2020

https://doi.org/10.5194/essd-2025-384
Preprint. Discussion started: 10 July 2025

and is based on daily ADT products with a horizontal resolution of $0.25° \times 0.25°$. Eddy detection and tracking are performed using an objective algorithm based on the closed-contour method combined with criteria such as amplitude and lifespan thresholds to ensure robust eddy identification. The dataset can be accessed from the AVISO+ website at: https://data.aviso.altimetry.fr/aviso-gateway/data/META3.1exp_DT/.

The RCLVs dataset used in this study is based on the work of Tian et al. (2022), who proposed an SLA-based orthogonal parallel detection method to identify rotationally coherent Lagrangian eddies at the global scale. Unlike traditional Eulerian eddy detection methods, this Lagrangian approach ensures material coherence by identifying vortices that maintain their structure and boundary over time, based on objective criteria derived from finite-time rotation. The RCLVs dataset is constructed from satellite-derived daily SLA fields with a $0.25° \times 0.25°$ resolution, covering the global ocean. The algorithm efficiently tracks eddies over time, providing information on eddy boundaries, lifetime, polarity, and coherent transport properties. The data include only vortices that meet strict rotational coherence conditions, making them particularly suitable for studies focusing on long-lived, materially coherent eddy structures. The dataset can be accessed from website at: https://data.casearth.cn/dataset/63369940819aec34df2674d7.

In this study, the Eulerian eddy dataset and the RCLVs dataset are used to compare the coherence with BHE through the advection of Lagrangian particles in them and their co-occurrence.

2.2 Methods

2.2.1 Identification of Black Hole Eddy

Black Hole Eddy, characterized by their boundaries undergoing minimal deformation during advection by the flow field, do not generate noticeable filamentous structures while in motion. The identification of these eddies employs a variational method, recognizing the boundaries as closed null geodesics defined by an appropriate Lorentz metric across the flow domain (Haller and Beron-Vera, 2013). The primary challenge lies in accurately pinpointing the boundaries that exhibit minimal deformation, which is indicative of the BHE. However, the resolution process is complex, resource-intensive, and inefficient, rendering it unsuitable for identifying eddies on a larger scale or over extended periods.

Serra and Haller (2017) presented a simplified and efficient algorithm for computing closed null geodesics that define coherent vortex boundaries in two-dimensional flows. Unlike earlier methods (Karrasch et al., 2015) that relies on direction field integration, singularity detection, and user-specified Poincaré sections, the proposed approach formulates a unified three-dimensional initial value problem that eliminates sensitivity to tensor field singularities and removes the need for manual input, enabling fully automated and robust vortex boundary detection. However, the algorithm's high computational demands and time-consuming process have hindered the production of a dataset of BHE. Our research presents an efficient automated extraction algorithm for Lagrangian eddies based on null geodesics. This method enhances and accelerates the existing null geodesics technique, thereby enabling the creation of a dataset of BHE in the North Pacific. In our experiment, the grid of initial positions ranges from 130° East longitude to 90° West longitude and from 0° to 50° North latitude.

https://doi.org/10.5194/essd-2025-384
Preprint. Discussion started: 10 July 2025

This research harnessed the powerful parallel processing capabilities of Graphics Processing Unit (GPU) to expedite and optimize the identification of BHE. We consider eddy detection to be a demanding data processing challenge. To accelerate recurring, large-scale computations, we partitioned them into numerous smaller GPU computational tasks. We generated Compute Unified Device Architecture (CUDA) code suitable for execution on NVIDIA GPU, thereby transferring the computational tasks to the GPU. This approach leverages the GPU's parallel processing capabilities for large-scale task execution. This paper utilizes CUDA as a multithreaded toolkit for GPU parallel computing. Figure 1 illustrates the workflow of the algorithm.

https://doi.org/10.5194/essd-2025-384
Preprint. Discussion started: 10 July 2025

Open Access Earth System Science Data Discussions

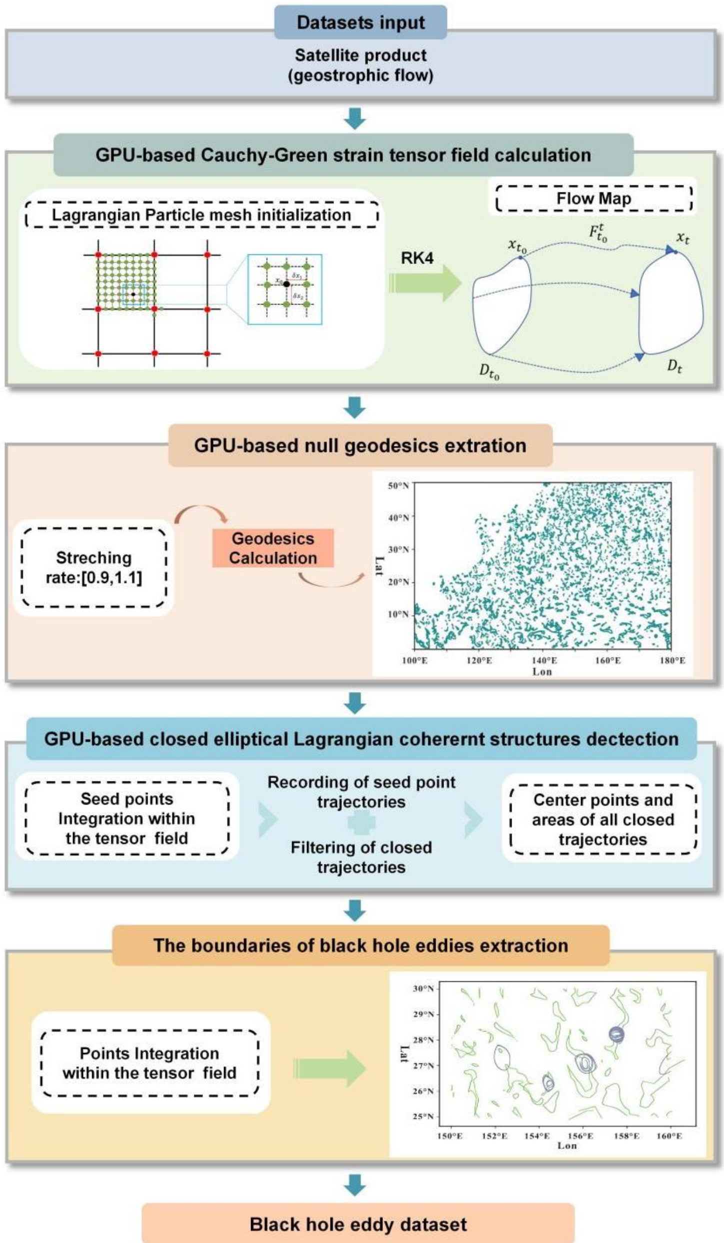

Figure 1. Flowchart of Black Hole Eddy(BHE) dataset generation based on satellite altimetry.

1. GPU-based Cauchy-Green strain tensor field calculation

Within the Lagrangian framework, we can express a two-dimensional unsteady flow field as follows:

$$\dot{x} = v(x,t), x \in U, t \in [t_0, t_1] \quad (1)$$

https://doi.org/10.5194/essd-2025-384
Preprint. Discussion started: 10 July 2025

Here, $v(x,t)$ denotes the velocity field at position x and time t, U signifies the boundary range of the flow field area, and the time interval $[t_0, t_1]$ represents the variation range of time t.

The flow map (Haller and Beron-Vera, 2013) can be elucidated as the trajectory of a fluid particle moving from its initial position x_0 at the initial time t_0 to its position x at time t:

$$F_{t_0}^{t}(x_0) := x(t; t_0, x_0) \tag{2}$$

We frequently utilize the Cauchy-Green strain tensor field to depict the forces exerted on Lagrangian particles in motion. The tensor field is expressed as follows:

$$C_{t_0}^{t_1}(x_0) = \left[\nabla F_{t_0}^{t_1}(x_0)\right]^T \nabla F_{t_0}^{t_1}(x_0) \tag{3}$$

In this context, ∇ symbolizes the Jacobian matrix of partial derivatives. The Cauchy-Green strain tensor, derived from the preceding computation, is positively definite. At any given point x_0, there will be two eigenvalues λ_1 and λ_2, along with two corresponding orthogonal eigenvectors ξ_1 and ξ_2. These are expressed as follows:

$$C_{t_0}^{t_0+T}(x_0)\xi_i(x_0) = \lambda_i(x_0)\xi_i(x_0), |\xi_i(x_0)| = 1, i = 1,2, 0 < \lambda_1(x_0) \leq \lambda_2(x_0) \tag{4}$$

In executing numerical simulations of BHE, our standard approach deploys a homogeneous grid structure throughout the flow field area, with the Cauchy-Green strain tensor computed at these grid nodes. As illustrated in Figure 1, we enhanced the accuracy of the simulation by densifying the original velocity field grid with a resolution of 1/4° by a factor of 8. The figure shows red solid nodes in the center, representing the main grid points. These are the input velocity field data points and serve as the primary computation locations for the Cauchy-Green strain tensor field. The green points surrounding them are the auxiliary nodes post-densification, and the black points correspond to the auxiliary grid point x_0. Following densification, we calculate the Cauchy-Green strain tensor for both the main grid points and auxiliary nodes. We set the distance between the grid points δ_{x_1} and δ_{x_2} to be 1/8 of the main grid point distance in this study, which is roughly equivalent to 1/32° when converted into degrees. This detailed grid configuration facilitates a more profound understanding and enhanced accuracy in simulating the dynamics of BHE. The spatial resolution stands at 1/32°, yielding a grid of $(140 \times 4 \times 8) \times (50 \times 4 \times 8)$, equating to dimensions of (4480×1600), and resulting in a total of 7,168,000 particles.

As depicted in Figure 1, the coordinates of x_0 are denoted as (x_i, x_j). Subsequently, the coordinates of the four auxiliary points around it can be represented as:

$$x_j^{up} = (x_j, y_j + \delta x_2),\ x_j^{down} = (x_j, y_j - \delta x_2) \tag{5}$$

$$x_j^{right} = (x_j + \delta x_1, y_j),\ x_j^{left} = (x_j - \delta x_1, y_j) \tag{6}$$

Once the flow field has advanced over time, we can ascertain the gradient value of the corresponding x_0 grid node map by determining the finite difference at the four densified auxiliary grid points around x_0:

$$\nabla F_{t_0}^{t_1}(x_j) \approx \left(\frac{F_{t_0}^{t_1}(x_j^{right}) - F_{t_0}^{t_1}(x_j^{left})}{2\delta x_1} \frac{F_{t_0}^{t_1}(x_j^{up}) - F_{t_0}^{t_1}(x_j^{down})}{2\delta x_2} \right) \tag{7}$$

https://doi.org/10.5194/essd-2025-384
Preprint. Discussion started: 10 July 2025

The incorporation of auxiliary points induces an eight times of the particle motion trajectories that must be calculated, hence heightening the computational complexity of the algorithm. In terms of computational speed, the workload at this stage is akin to directly doubling the resolution in both horizontal and vertical directions on the main grid points. However, the utilization of auxiliary points allows for control over the calculation precision of $\nabla F_{t_0}^{t_1}(x_j)$. Specifically, by altering the dimensions of δ_{x_1} and δ_{x_2}, we can modulate the precision of the main grid node mapping's gradient value. This method effectively mitigates the noise in the eigenvector field and addresses the issue of numerical sensitivity to alterations in the eigenvector direction (Serra and Haller, 2017).

Given the three-dimensional nature of the flow field — encompassing longitude, latitude, and time-as particles move, they necessitate interpolation. Striving for an optimal balance between precision and computation speed, we employ the Cubic interpolation method and use B-splines as the mixing matrix. The Cubic interpolation method provides third-order spline interpolation, thereby ensuring high-order continuity of the velocity field post-interpolation and circumventing significant errors induced by numerical sensitivity.

When calculating the tensor field and setting up the initial particle grid, we ensured a unique correlation between particle points and threads to maintain computational accuracy. Based on the GPU's computational capacity, once the size of the initial grid($(m \times k) \times (n \times k)$) and the number of threads per Block in the GPU ($m \times n$) are inputted, the size of the Block to be allocated for each Grid ($k \times p$) can be determined. After thread allocation, the auxiliary points moving in the flow field use a GPU-accelerated fourth-order Runge-Kutta integration (RK4) to obtain the advection of Lagrangian particles. To secure sufficient computational precision, it is imperative to curtail the time step to the greatest extent feasible. Bearing computational capability in mind, we settled on a time step of 0.1 days for this study. Upon acquiring the gradient matrix, we derive the Cauchy-Green strain tensor by multiplying the transpose of the gradient matrix by itself. We then compute the partial derivatives of the Cauchy-Green strain tensor. This procedure constitutes a pivotal step in our investigation of BHE, and it lays a crucial theoretical groundwork for subsequent numerical simulation. The RK4 procedure and tensor field computation are integrated within a CUDA-recognizable function and are recursively called in each thread. Once all threads have completed their tasks, the program consolidates the output data and transmits it to the host at each timestep. Logically, this multi-threaded, GPU-based parallel algorithm diminishes the computational complexity from $O_{(o)}$ to $O_{(o/p)}$, where p signifies the count of threads running on the GPU.

2. GPU-based null geodesics extraction

For the variational problem:

$$Q[\gamma(s)] = \int_{\gamma} L\big(x(s), x'(s)\big) ds \tag{8}$$

There exists a quadratic Lagrangian function:

$$L(x, x') = \frac{1}{2}\langle x', A(x)x' \rangle \tag{9}$$

https://doi.org/10.5194/essd-2025-384
Preprint. Discussion started: 10 July 2025

where $A(x)$ is a tensor within the study area, $\langle \cdot,\cdot \rangle$ denotes the Euclidean inner product, and the parameterized expression of the geodesic λ is:

$$gx(x', x') = \frac{1}{2}\langle x', A(x)x' \rangle \tag{10}$$

A geodesic is existent when the Euler-Lagrange equation is satisfied:

$$\frac{1}{2}\nabla_x \langle x', A(x)x' \rangle - \frac{d}{ds}[A(x)x'] = 0 \tag{11}$$

In the computational procedure, Equation 11 can be incorporated into the earlier mentioned expression to derive the geodesics. We define the stretch rate λ within the range of [0.9, 1.1], employing a sampling interval of 0.025. Each discrete λ yields a corresponding geodesic calculation. In the process of calculating geodesics and extracting null geodesic contours, the original algorithm is inefficient, as it requires significant time to compute and traverse each contour individually. However, since these contours are independent of one another, we can enhance the computation process by employing a GPU parallel acceleration algorithm. In this approach, each thread corresponds to a single geodesic line, allowing for simultaneous calculations and significantly reducing processing time. Utilizing a polar coordinate system, the partial derivatives of the tensor field calculated in equation are used as inputs, the computation steps for the null geodesic field adhere to the following equation:

$$ZeroSet = C^{11}(x)cos^2\emptyset + C^{12}(x)sin2\emptyset + C^{22}(x)sin^2\emptyset - \lambda^2 \tag{12}$$

In the equation, ∅ is the rotation angle. Importantly, given that the Lagrangian vortex forms a closed curve in polar coordinates and its boundary completes a full rotation, we can assign $\phi = 2\pi$. The curve meeting the condition $ZeroSet = 0$ earns the definition of a zero geodesic. The application of this computational methodology significantly enriches our comprehension and simulation of BHE.

3. GPU-based closed elliptic Lagrangian coherent structure detection

The assemblage of zero geodesics derived from the aforementioned step 2 is denoted as ZeroSet and is segmented into various seed points. Subsequently, these seed points undergo integration within the mixed tensor field, which is defined as follows:

$$x' = e_\emptyset \tag{13}$$

$$\emptyset' = -\frac{cos^2\emptyset\langle \nabla_x C^{11}(x), e_\emptyset \rangle + sin2\emptyset\langle \nabla_x C^{12}(x), e_\emptyset \rangle + cos^2\emptyset\langle \nabla_x C^{22}(x), e_\emptyset \rangle}{sin2\emptyset[C^{22}(x) - C^{11}(x)] + 2cos2\emptyset C^{12}(x)} \tag{14}$$

Within this context, ϕ continues to represent the rotation angle. Similar to the tensor field computation in step 1 and the geodesic calculation in step 2, we use the GPU parallel acceleration algorithm for seed point integration. To achieve closed Lagrangian curves as anticipated, the value of ϕ is designated as 2π. Ultimately, this will result in a sequence of nested closed curves, jointly constituting an elliptical Lagrangian coherent structure.

It is essential to recognize that not all points on the null geodesics can be integrated within the tensor field to produce closed curves. Only a subset of the seed points on the null geodesics undergo integration within the tensor field, leading to nested closed vortex curves. Additionally, the quantity of layers in these nested curves is variable, ranging from a single layer to multiple ones.

Furthermore, establishing certain thresholds is necessary to discern whether the integrated curves create closed, nested boundaries. This process involves more than just calculating the distance between the curve's start and end points. It also necessitates the computation of the corresponding rotation angles, denoted as ϕ, for these points. Should the differential equal 2π, we can then classify the boundary as a fully enclosed, nested vortex boundary.

4. The boundaries of Black Hole Eddy extraction

We employed an algorithm aimed at discerning the outermost boundary from an assembly of nested, closed, elliptical Lagrangian coherent structures, deemed as the boundary of the BHE (He et al., 2022). Figure 2 illustrates a suite of closed, elliptical Lagrangian coherent structures where the central points P1 to P6 are not perfectly aligned, precluding determination of the outermost boundary through simple area comparison of the polygons. This process involves the subsequent steps:

(1) Calculate the centroid of all the elliptical Lagrangian coherent structures acquired in the prior step.

(2) Execute clustering predicated on the distances between centroids to procure the collection of centroids belonging to the same nested set of Lagrangian coherent structures. This aligns with P1 to P6 in Figure 2.

(3) Compute the areas S1 to S6 of the Lagrangian coherent structures corresponding to P1 to P6, and identify the elliptical Lagrangian coherent structure with the maximum area as the Lagrangian Eddy boundary.

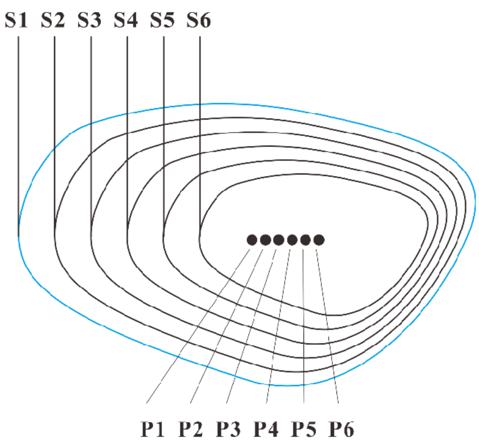

Figure 2. The outermost boundary of the elliptic Lagrangian continuum. p1 - p6 are the centers of mass of the nested elliptic Lagrangian continuum, and s1 - s6 are the areas of the nested elliptic Lagrangian continuum, respectively.

2.2.2 Tracking of Black Hole Eddy

https://doi.org/10.5194/essd-2025-384
Preprint. Discussion started: 10 July 2025

On account of the strong coherence of BHE boundaries, following the advection pathway of a single particle was sufficient to track coherent water masses between the 7 d timesteps (Jones-Kellett and Follows, 2024). In this study, we transforms the vortex tracking problem into a vortex-centered advection problem and automates the tracking algorithm(Figure 4), the algorithm proceeds as follows:

(1) Input data: The algorithm starts by ingesting Black Hole identification data obtained through from January 1, 1993 to May 5, 2023.

(2) Eddy core advection: Using a GPU-parallelized RK4 algorithm (as detailed in Section 2.2.1), the coordinates of eddy cores are computed for each time step. These coordinates are then linked to form the advection trajectories of BHE within each day(Figure 3).

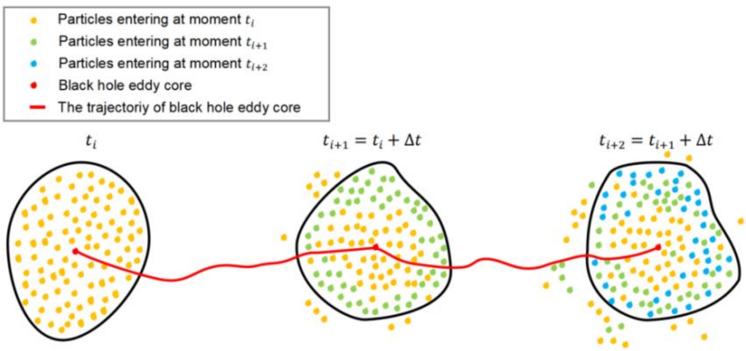

Figure 3. Schematic diagram of the advection eddy core (red) connecting the BHE trajectories.

(3) Candidate matching using K-D tree: To facilitate efficient spatial matching, a K-D tree partitions the space. For each time step, candidate BHE is identified within a standard circular region (radius is 1.5 °, exceeding the maximum daily displacement) centered on the eddy core.

(4) Segment tracking: For consecutive time windows, each candidate BHE is evaluated. If the advected eddy core from Day t_i falls within the boundary of any candidate BHE on Day t_{i+1}, the BHE from Day t_i is marked as "live" and further checks for that core are bypassed to expedite matching. If no matches are found, the BHE is marked as "death" indicating the end of the tracking segment.

(5) Time window progression: The tracking process iterates through time, sliding the window forward until all segments between January 1, 1993 and May 5, 2023 are processed.

(6) Branch construction: Segments marked as "live" are sequentially linked into a branch until a "death" status is encountered. Each branch represents the complete life cycle of BHE, with the final output comprising the full temporal branches of tracked eddies.

https://doi.org/10.5194/essd-2025-384
Preprint. Discussion started: 10 July 2025

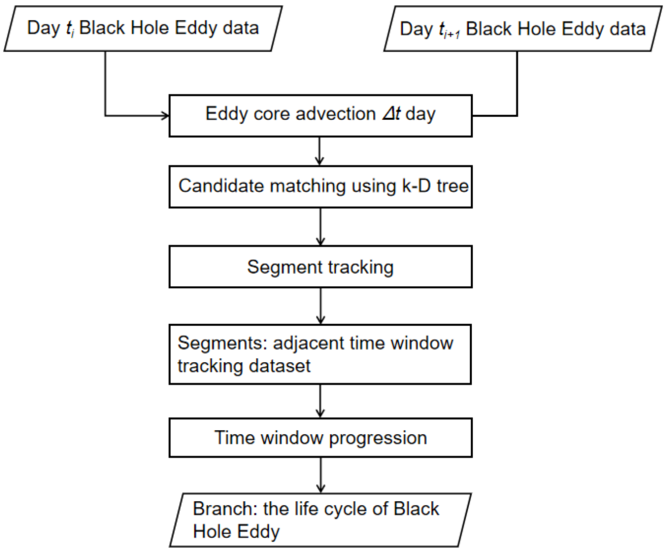

Figure 4. Flowchart of the eddy core advection tracking algorithm.

2.2.3 Algorithm efficiency analysis

Using the efficient BHE identification algorithm based on GPU parallel acceleration in Section 2.2, this study is planned to generate the North Pacific Black Hole Eddy dataset for a total of 30 years from 1993-2023. The computer configurations used during the BHE dataset computation were Intel(R) Core(TM) i7-10700 CPU @ 2.90GHz and NVIDIA GeForce RTX 3060 12GB. The algorithms were compiled and implemented in Python 3.8 (Anaconda 3), and CUDA in NVIDIA graphics card was used (v11.0) for GPU acceleration. All the experiments in this paper as well as the dataset generation were done using this computer configuration.

Take the example of calculating the BHE on January 1, 2021 with a T = 30-day, Figure 5 shows the time used and the percentage of time in each part for the original method and the GPU-accelerated algorithm of this paper in calculating the BHE. It can be seen that before the optimization and acceleration of the algorithm, the null geodesics computation and the nested closed eddy boundary set computation occupy most of the time consumed in the original method, with a time share of 50.79% and 27.09%, respectively, and the tensor field computation part is also higher, with a time share of 18.14%. These three parts take up the majority of the time for identification. However, after GPU acceleration, it can be seen that for the eddy identification on the same day, the identification method in this paper significantly reduces the time used in each part of the identification of BHE. The time used in the tensor field computation part and the geodesic line computation part are about 1/15 of the original time, and the total time used is about 7 min, which greatly shortens the computation time. However, the acceleration of the Black Hole vortex boundaries extraction is not as significant, because this is the smallest part in terms of time and percentage in the original method, which suggests that this is not a key step in the algorithm's efficiency, and there is less room for speedup than the other parts. Moreover, screening each boundary in the outermost closed boundary of the BHE and performs a large number of I/O operations to write the results to files, so that the bottleneck of the storage

https://doi.org/10.5194/essd-2025-384
Preprint. Discussion started: 10 July 2025

device can constrain the acceleration results. However, after GPU acceleration, the duration of this part has been as low as 68s, which is well within the acceptable range.

With the optimization of the GPU acceleration process, the overall time consumption of the whole set of identification algorithms proposed in this paper is only about 1/13 of that of the original null geodesic algorithm. At this computational speed, generating 30 years of BHE data on a daily basis takes about 51 days, compared to 662 days using the original algorithm, thereby enabling the construction of a large-scale, long-term BHE dataset.

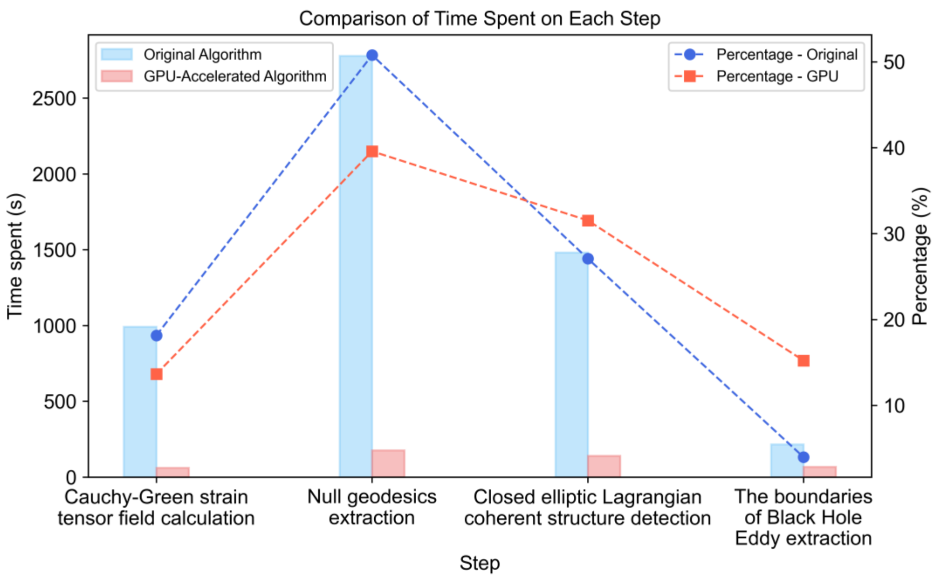

Figure 5. Comparing the efficiency of GPU-accelerated algorithms and original methods

3 Results

3.1 Description of eddy dataset

BHE v1.0 consists of two components. First, the general features of coherent eddies are detailed in the directory named "Eddyidentification". The information regarding 30-day and 90-day eddies is stored separately in three JSON files, each containing the relevant data.

key : the name of the BHE.

Eddy ID: Indexing: the eddies identifies the date, which is indexed in ascending order starting from 0.

Eddy Centroid: the longitude (in degrees East) and latitude (in degrees North) of the eddy center, with a frequency of 7 days.

lon, lat : the longitude and latitude of the BHE boundary.

Eddy Area: the area of the BHE.

Eddy Types: types of BHE, including Cyclonic and Anticyclonic.

Eddy Radius: the radius of the BHE.

https://doi.org/10.5194/essd-2025-384
Preprint. Discussion started: 10 July 2025

Lam: the stretch rate associated with each BHE.

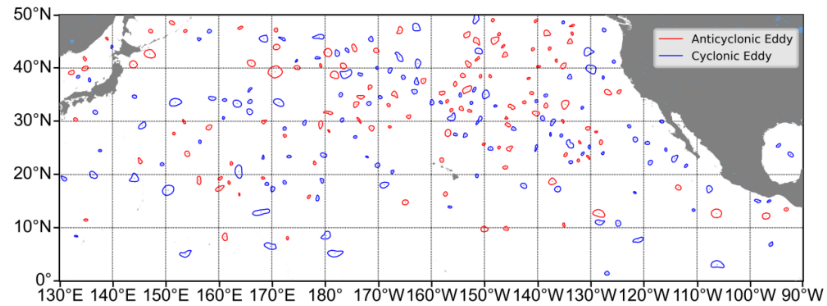

Figure 6. 30-day Black Hole Eddies (BHEs) extracted from Lagrangian particles initialized on 4 June 2021.

Second, the trajectories of the BHE boundaries are provided in the directory named "Eddytrajectory". This represents the first attempt at creating an open-source BHE dataset. We utilize a Pickle file containing a three-dimensional array to store the core and the boundary every 7 days for each eddy. This dataset provides 18387 with radius larger than 20 km and lifetimes longer than 4 weeks.

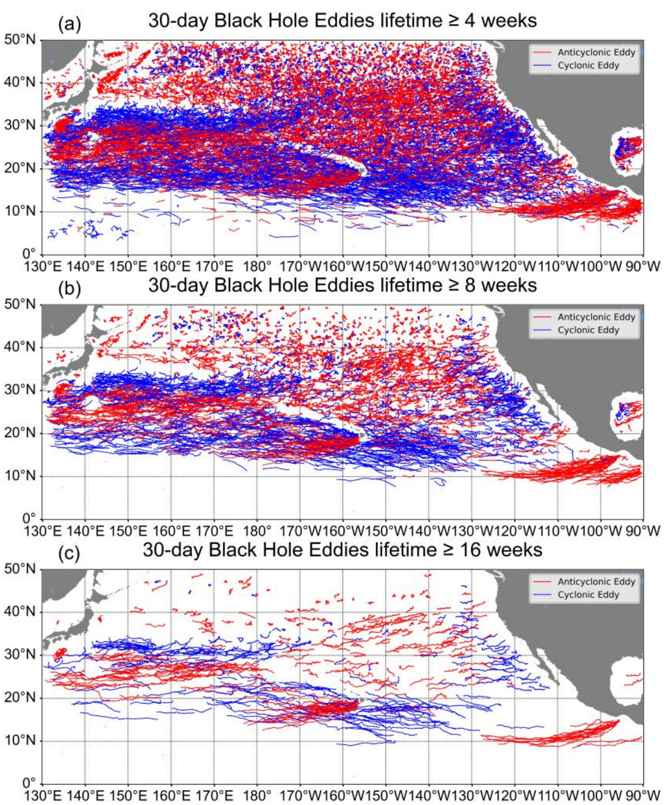

Figure 7. The trajectories of cyclonic (blue lines) and anticyclonic (red lines) BHEs over the 30-year period Januaray 1993-May 2023 for (a) lifetimes ≥ 4 weeks and (b) lifetimes ≥ 8 weeks and (c) lifetimes ≥ 16 weeks.

https://doi.org/10.5194/essd-2025-384
Preprint. Discussion started: 10 July 2025

3.2 Analysis of the strong coherence of Black Hole Eddy

We randomly initialized Lagrangian particles within Black Hole anticyclonic\cyclonic eddy on January 1 and tracked their movement over time(Figure 8 and Figure 9). At the initialization (Figure 8a and Figure 9a), the yellow\purple particles are located inside the Eulerian anticyclonic\cyclonic eddy boundary but outside the anticyclonic\cyclonic RCLVs, while the pink\green particles are situated within the anticyclonic\cyclonic RCLVs but outside the Black Hole anticyclonic\cyclonic eddy. In the case of Eulerian anticyclonic eddy, distinct vortex filaments begin to develop on 15 January (Figure 8b), just two weeks after initialization. These filaments extend and wrap outward, indicating that material inside the Eulerian boundary begins interacting with the surrounding environment shortly after initialization. After 30 days advection, the deformation intensifies, leading to a complete loss of the eddy's coherent structure and extensive mixing with surrounding waters. For anticyclonic RCLVs, filamentary structures appear slightly later. After 30 days advection (Figure 8c), clear signs of deformation can be observed, as particles begin to stretch and form elongated structures outside the anticyclonic RCLVs boundary. Although the anticyclonic RCLVs demonstrate stronger material retention than Eulerian eddies, they too undergo gradual mixing, and after 90 days (Figure 8e), the filaments become prominent, indicating a loss of coherent transport. In contrast, anticyclonic BHE maintains its coherent structure throughout the entire tracking period. The anticyclonic BHE boundary serves as an effective barrier to material transport, firmly enclosing particles and preventing exchange with the surrounding fluid. Even after four months (Figure 8f), particles within the BHE remain tightly bound, and no filamentation or mixing is observed. Example of cyclonic eddy also reveals the same phenomenon (Figure 9).This comparison highlights the strong material coherence of BHEs over Eulerian eddies and RCLVs. The region between the RCLV and Eulerian eddy boundaries can be considered a transition zone, where eddy-like motions occur but without coherent material retention. Recognizing such spatial distinctions helps refine our understanding of mesoscale eddy structure and provides a pathway for exploring submesoscale dynamics embedded within these systems.

https://doi.org/10.5194/essd-2025-384
Preprint. Discussion started: 10 July 2025

Open Access Earth System Science Data Discussions

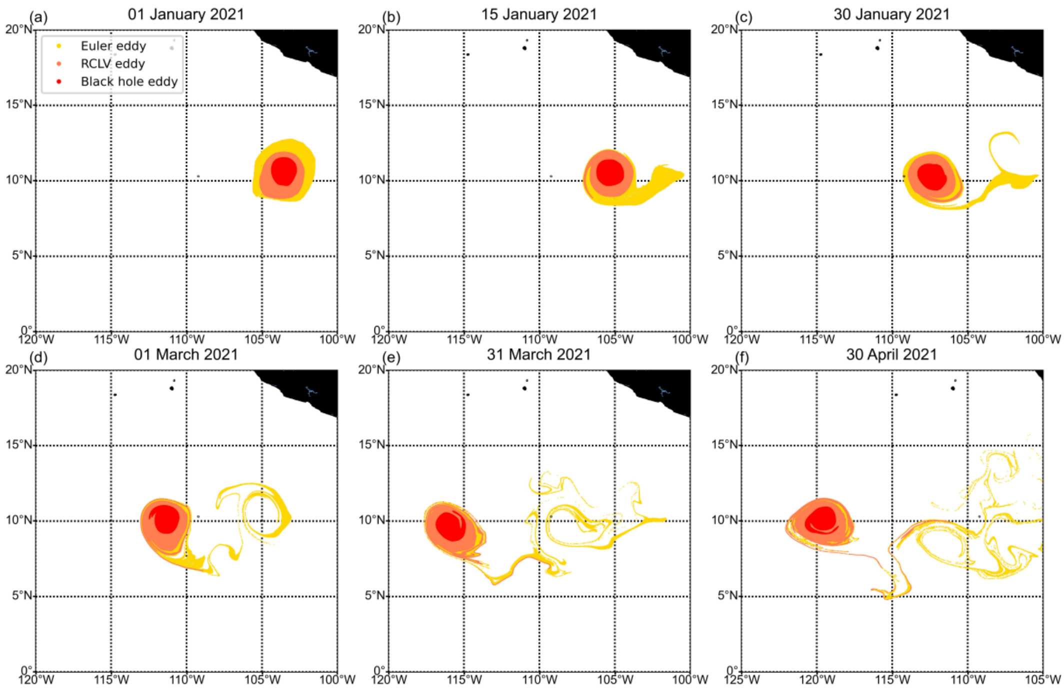

Figure 8. The particles advection trajectories for anticyclonic BHE, Euler eddy and rotationally coherent Lagrangian vortices (RCLVs). (a) - (f) The advection results for the initial position, 15, 30, 60 ,90 and 120 days of advection, respectively.

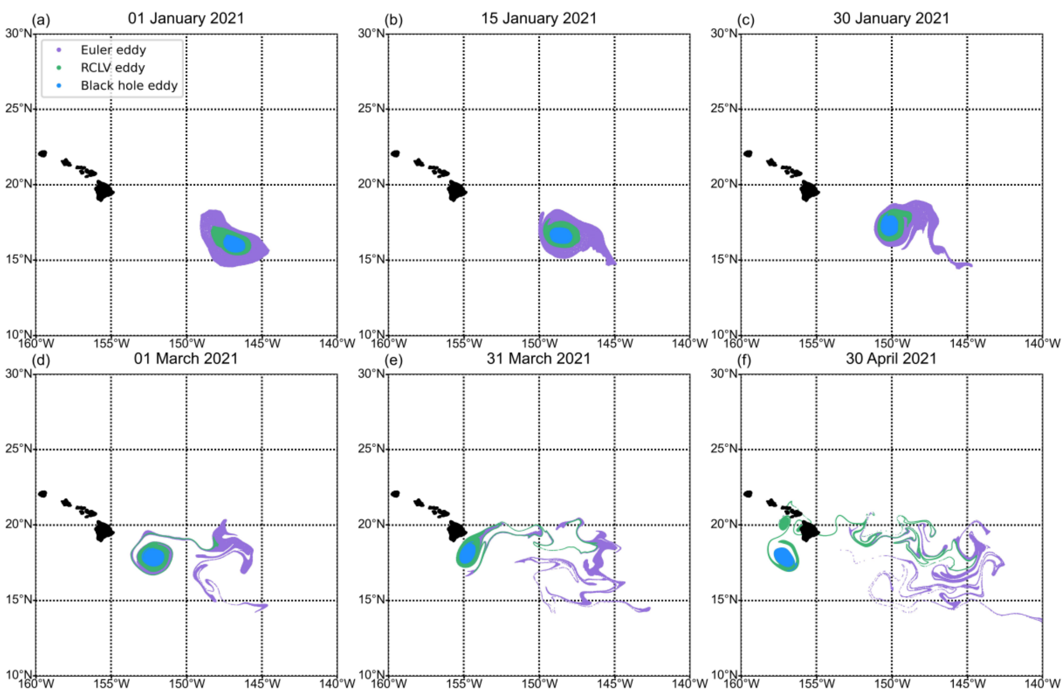

Figure 9. The particles advection trajectories for cyclonic BHE, Euler eddy and RCLVs. (a) - (f) The advection results for the initial position, 15, 30, 60 ,90 and 120 days of advection, respectively.

https://doi.org/10.5194/essd-2025-384
Preprint. Discussion started: 10 July 2025

3.3 Relationship of Black Hole Eddies, RCLVs and Eulerian eddies

Figure 10 illustrates the frequency of instances of different types of eddies and their distribution proportions within both cyclonic and anticyclonic categories, as well as their overlapping and non-overlapping occurrences. The simultaneous presence of the three eddy types—BHE, Euler eddy, and RCLVs—is predominantly characterized by cyclonic occurrences (71.28%) and anticyclonic occurrences (71.02%). In contrast, the Naked Black Hole Eddy are eddies that neither overlap with SLA eddies nor with RCLVs, comprising 6.12% of cyclonic and 6.74% of anticyclonic instances. We randomly load two data records to show the particle positions during the eddy lifetime (Figure 11 and Figure 12). An interesting phenomenon is that the eddy in Figure 11a and Figure 12a is not initially located around a closed SLA contour or LAVD contour, but a coherent structure does exist. This type of coherent eddies are all neglected when using the Eulerian method and LAVD method. The results show that 14 days after the advection of the vortex (June 18), the Eulerian eddy and RCLVs have been severely deformed, with filamentary structures appearing and starting to mix with the background ocean current field; 28 days after the advection (July 2), the filamentary structure of the Eulerian eddy and RCLVs further develop into an elongated ribbon, which are completely integrated with the ocean water, and the eddy morphology has ceased to exist. Unlike the Eulerian eddy and RCLVs, the Naked Black Hole Eddy remains strongly coherent throughout its life cycles. Although the Naked Black Hole Eddy rotates and moves horizontally during the motion of the flow field, no filamentary structure appears at the eddy boundary, and the particles inside the eddy remain firmly wrapped within the eddy boundary without dispersing or escaping to the surrounding ocean, which proves that the strong coherence of Naked Black Hole Eddy.

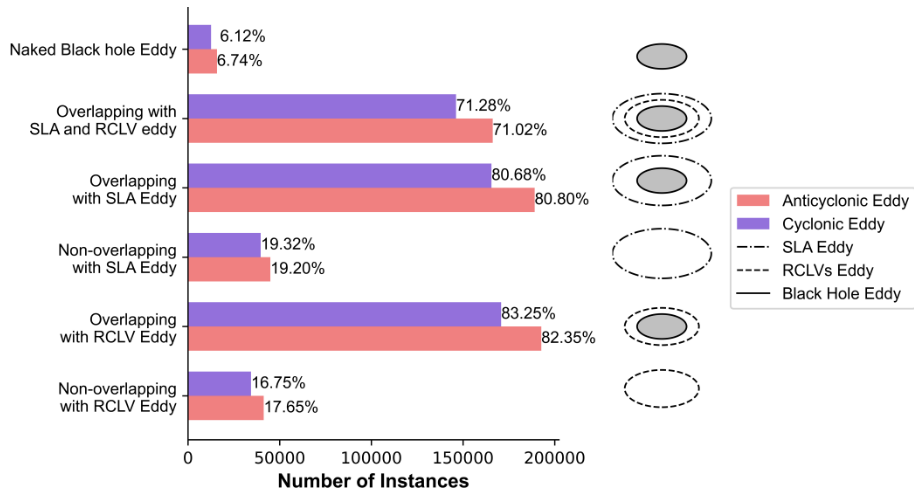

Figure 10. The number of BHE that are concurrent (overlapping) and not concurrent (non-overlapping) with the other eddy. The percentages of eddies exhibiting the given characteristic compared with the total number of eddies of each polarity. The Naked Black Hole Eddy are eddies that neither overlap with SLA eddies nor with RCLVs.

https://doi.org/10.5194/essd-2025-384
Preprint. Discussion started: 10 July 2025

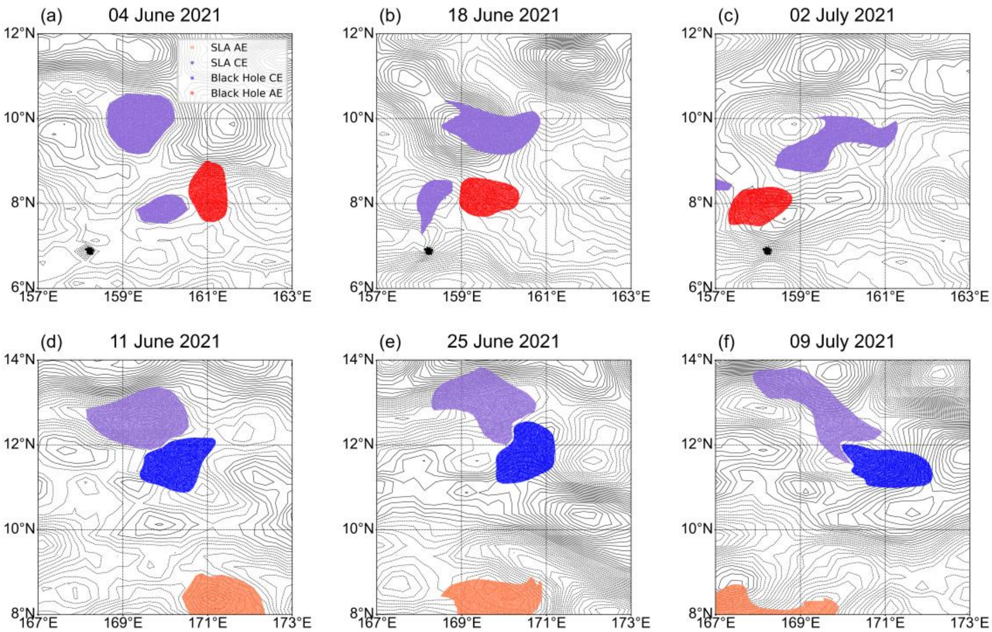

Figure 11. Positions of particles (colored dots) inside the BHE boundary and the SLA eddy boudary every 14 days. The ADT fields are overlaid using black contours with solid lines for positive values and dashed lines for negative values.

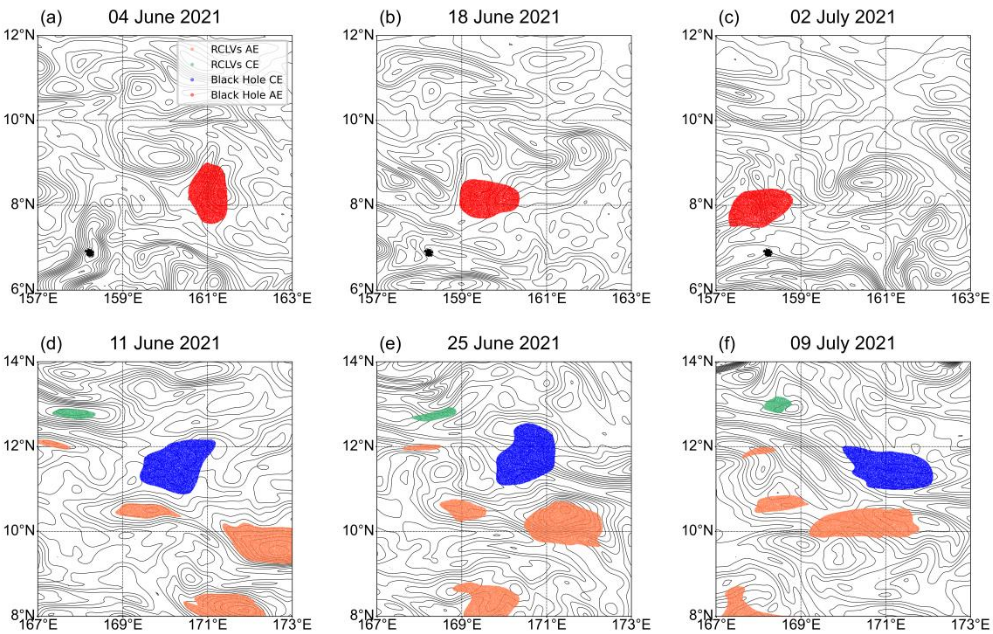

Figure 12. Positions of particles (colored dots) inside the BHE boundary and the RCLVs boudary every 14 days. The background is the LAVD fields.

3.4 Geographic and temporal distribution of Black Hole Eddy

https://doi.org/10.5194/essd-2025-384
Preprint. Discussion started: 10 July 2025

3.4.1 Geographic distribution

We assessed the geographic distribution of the BHEs across the North Pacific Ocean. In Figure 13a, eddy frequency was calculated from the number of times each BHE core and RCLVs eddy core within 1° × 1° grids over 30 years. Compared with RCLVs, the number of BHE is lower, mainly in the Kuroshio Extension (30°N-40°N) and the subtropical region of the northeastern Pacific Ocean (30°N-50°N), and the eddies generated at low latitudes (below 10°N) are very few(Figure 13a). The number of eddies identified by RCLVs is much higher than that of BHE, especially in the subtropical countercurrent (15°N-25°N) and the California coastal current(Figure 13b) . This is because the RCLVs method favors eddies with low coherence, while the BHE method is more rigorous and mainly identifies strongly coherent eddies (Haller and Beron-Vera, 2013; Haller et al., 2016).

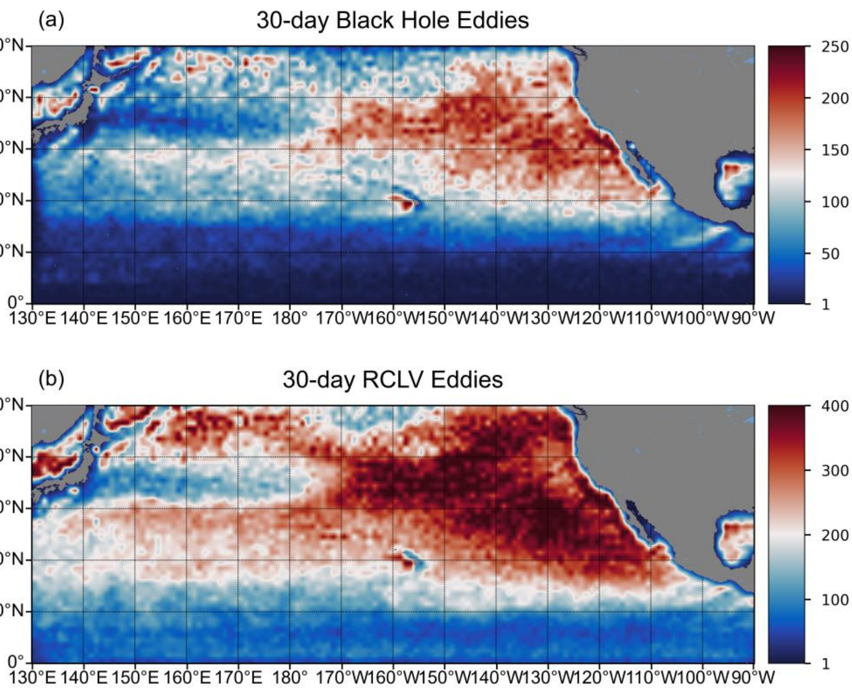

Figure 13. The geographic distribution of eddy numbers in 1° × 1° **grids from 1993 to 2023 for (a) BHE and (b) RCLVs.**

The polarity probability (P) is defined $P = \frac{(F_A - F_C)}{(F_A + F_C)}$, where F_A is the frequency of anticyclones, and $F_C$is the frequency of cyclones (Chaigneau et al., 2008). When $P > 0$ ($P < 0$), anticyclonic (cyclonic) eddy polarity is more common at the given location. Figure 14 shows the geographic distribution of polarity probability of BHE and RCLVs. Compared to the relatively uniform anticyclonic polarity of RCLVs, BHE exhibits greater spatial variability in polarity probability across latitudes. Especially, the polarity distribution of the BHE (Figure 14a) is strongly anticyclonic (red) in the region north of 30°N, and more cyclonic (blue) between 10°N and 25°N. This distribution pattern is associated with the shear structure of the Kuroshio,

https://doi.org/10.5194/essd-2025-384
Preprint. Discussion started: 10 July 2025

Open Access Earth System Science Data Discussions

baroclinic instability, and other dynamical processes (Chelton et al., 2011b)(Chelton et al., 2011b). Previous studies (Qiu et al., 2014; Wu and Gan, 2023; Jia et al., 2011) have shown clearly that the Hawaiian Lee Eddies generate the strongest signals of two distinct groups of eddy activity in this domain. BHE also reveals two stark Lee Eddy pathways depending on the polarity, whereas RCLVs Lee Eddies have a more diffuse polarity probability. This is due to the fact that wake eddies exhibit dipole structure (cyclone-anticyclone pairs) in response to current shear and wind stress (Travis and Qiu, 2017).

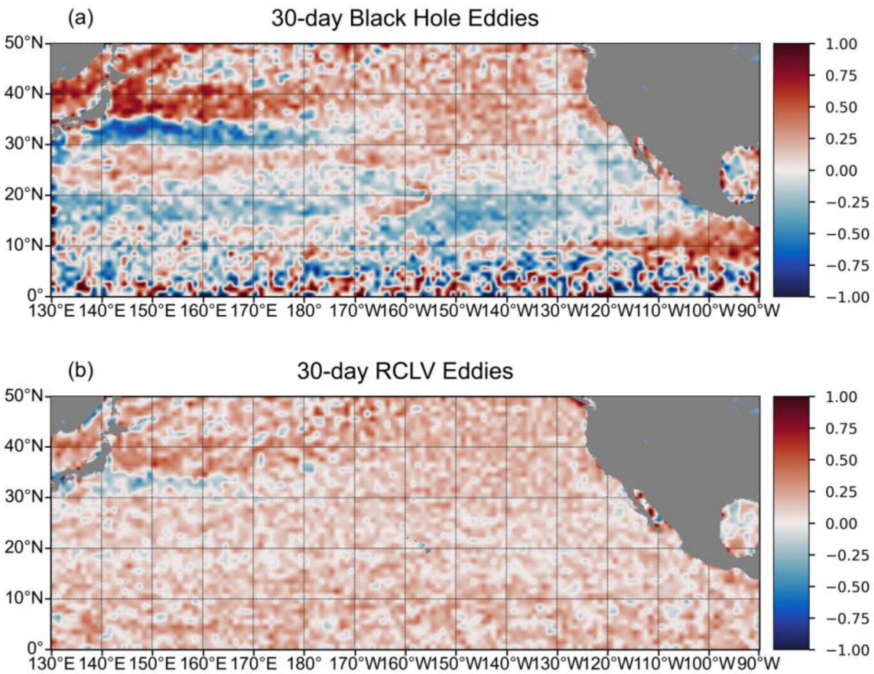

Figure 14. Polarity probability in 1° × 1° grids from 1993 to 2023 for (a)BHE and (b) RCLVs. $P < 0$ (blue) indicates more cyclonic activity, and $P > 0$ (red) more anticyclonic activity.

3.4.2 Temporal distribution

As demonstrated in Figure 15a, BHEs and RCLVs have similar interannual trends. However, the RCLVs method identifies more eddies than the BHE method suggests. This indicates that the RCLVs identification method is more likely to capture a larger number of long-lived eddies. In contrast, BHE method may have a higher coherence requirement, leading to the identification of fewer eddies. For BHE, there are more anticyclonic eddies than cyclonic eddies, corresponds to the global distribution of previous statistics (Chelton et al., 2011b)(Chelton et al., 2011b), while the opposite is observed for RCLVs. The monthly average eddy frequency data shown in Figure 15b reveals peaks in July and August, while the lowest frequencies occurring in January and February. This pattern is consistent with previously noted summer peaks of eddy kinetic energy in subtropical gyres (Zhai et al., 2008).

https://doi.org/10.5194/essd-2025-384
Preprint. Discussion started: 10 July 2025

Earth System Science Data
Open Access
Discussions

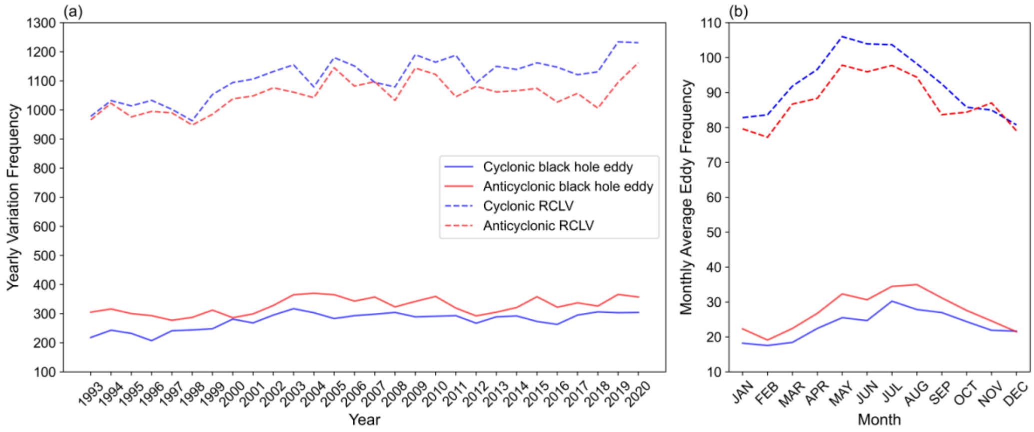

Figure 15. (a) BHE and RCLVs rolling mean frequency from 1993 to 2020. Frequency refers to the number of eddies per 7 day time step. (b) Monthly average BHE and RCLVs frequency.

3.5 Black Hole Eddy characteristic statistics

3.5.1 Eddy size

Figure 16 illustrates the distribution of eddy radius across different latitude zones. In Figure 16a, the mean eddy radius (dashed line) exhibits a clear decreasing trend from low to high latitudes, particularly at latitudes of 40° and above, where the eddy radius becomes notably smaller and more concentrated. In contrast, the eddy radius of the RCLVs, shown in Figure 16b, varies within a relatively small range and does not display a clear monotonic trend, indicating that it is weakly influenced by latitude. The BHE demonstrates larger and more dispersed radius at lower latitudes, which progressively decrease and become more consistent as latitude increases. These latitudinal differences in the BHE radius may be linked to variations in geostrophic balance and Coriolis force (Chelton et al., 2011b)(Chelton et al., 2011b). At low latitudes, where the Coriolis force is weaker, eddies are more likely to develop larger radius, while at higher latitudes, the strengthening Coriolis force leads to smaller and more constrained eddy radius.

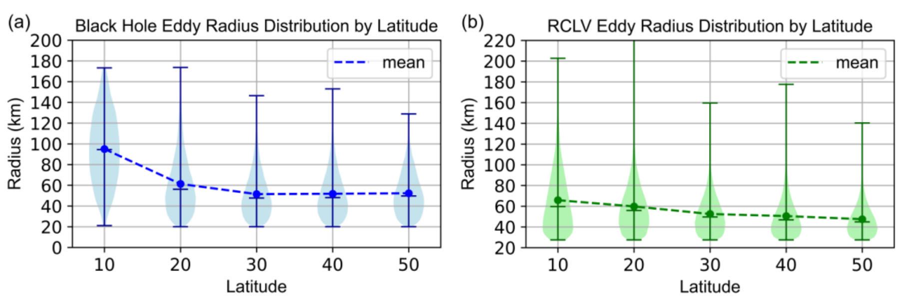

Figure 16. Statistics of radius for BHE and RCLVs. The box plot shows statistics of all eddies in 10° bins. The box and the whisker span the min value to the max of the distribution. The line in the box indicates the median. The means of all eddies in a bin are shown using dashed lines, blue for BHE and green for RCLVs.

https://doi.org/10.5194/essd-2025-384
Preprint. Discussion started: 10 July 2025

3.5.2 Eddy lifetime

We presents a comparative analysis of the BHEs and RCLVs in terms of their joint probability density distributions of lifetime and radius. The results indicate that both eddy types exhibit similar lifetime distributions, predominantly concentrated within the range of 4-6 weeks, with RCLVs displaying slightly higher probability densities, suggesting a greater tendency toward shorter lifetimes. In terms of eddy radius, RCLVs have a slightly larger peak radius (51.39 km) compared to BHEs (44.52 km), yet their overall distribution patterns remain similar, with the majority of eddies falling within the 30-70 km range. Further joint probability density analysis reveals that BHEs more focus on coherent small eddies, while RCLVs are more concentrated in the long-lifetime region, potentially select eddies with longer lifetimes and larger radius.

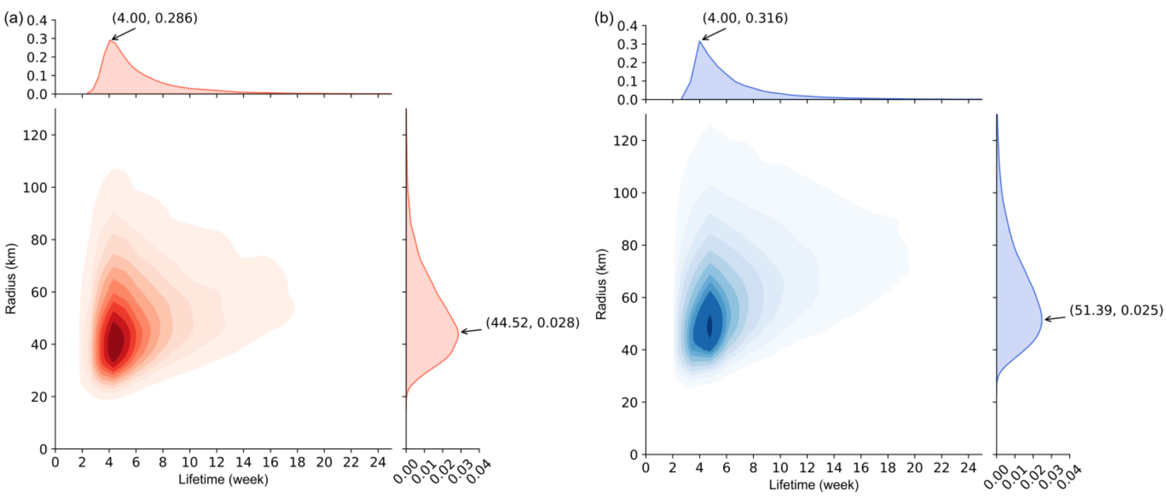

Figure 17. Joint probability density distributions of lifetime and radius for BHEs (a, red) and RCLVs (b, blue). The contour plots represent the density distributions, while the marginal density plots on the top and right illustrate the probability distributions of lifetime and radius, respectively.

3.6 Transport water by Black Hole Eddy

Following the methods used by and Zhang et al. (2014), we calculate the averaged zonal and meridional transport across the section for each $1° \times 1°$ grid by $Q_x = \frac{\sum V \cdot C_x}{N \cdot D_x}, Q_y = \frac{\sum V \cdot C_y}{N \cdot D_y}$, where V, $C_x(C_y)$, and D are the volume, zonal (meridional) propagation speed, and lifetime of an eddy in days, respectively. $\sum$ means the integration of all eddies over the studying period N in days, and $D_x(D_y)$ is the length of one longitude (latitude) degree. The eddy volume is calculated by $V = s\pi R^2 h$, where R is the eddy radius, s = 0.5 is a correction factor for the eddy vertical structure from Dong et al. (2014), and h = 500 m is the eddy depth. Here, BHEs and RCLVs only include eddies that are 28 days are considered from 1993 to 2020.

As shown in Figure 18, both eddy types contribute predominantly westward (negative) zonal transport across the North Pacific basin. However, BHEs exhibits notably weaker westward transport intensity compared to RCLVs, particularly between 10° N and 30°N (Figure 18a and Figure 18c). In contrast, the meridional transport patterns (Figure 18b and Figure

https://doi.org/10.5194/essd-2025-384
Preprint. Discussion started: 10 July 2025

Open Access Earth System Science Data Discussions

18d) reveal a more diffusive and spatially scattered signal for RCLVs, with alternating northward and southward fluxes. Meanwhile, BHEs show relatively coherent southward transport signals, especially in the eastern tropical Pacific. The meridionally-integrated zonal transport profiles (Figure 19a) further confirm that Black Hole Eddies induce a consistent but weaker westward transport compared to RCLVs. The peak value of meridionally-integrated zonal transport by BHE is only about 1.5 Sv, which is three times smaller than that of the RCLVs. In the meridional direction (Figure 19b), BHEs and RCLVs exhibit similar latitudinal trends, with prominent peaks around 10°N and 30°N, yet RCLVs also show enhanced variability and higher transport intensity in several latitude bands. However, the meridional transport of the BHEs is slightly stronger than that of the RCLVs near 40°N. This is because at near 40°N, eddies are often strongly sheared by Kuroshio Extension and tend to be stretched into non-circular, north-south eccentered structures (Early et al., 2011). RCLVs emphasizes the consistency with the center of rotation, and tends to identify "compact" rotating eddies, thus easily omitting those structures that are elongated by shear but still have transport functions (Haller, 2015; Beron-Vera et al., 2013).

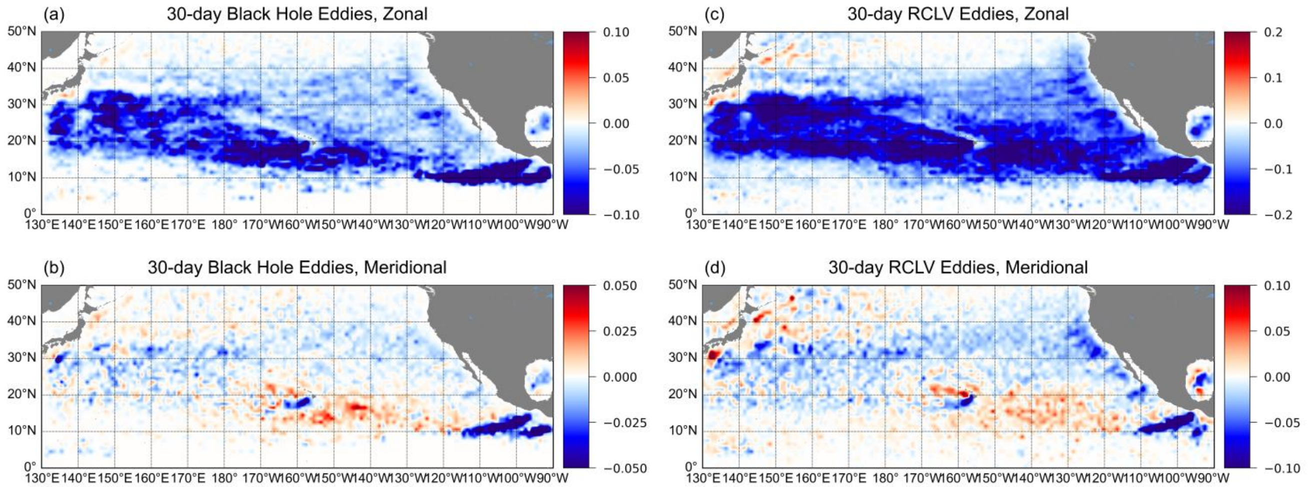

Figure 18. The Northern Pacific distribution distributions of the (a, c) zonal and (b, d) meridional transport by (a, c) BHEs and (b, d) RCLVs in 1° × 1° bins. Note that different colorbar ranges are used here and the transport unit is the sverdrup [Sv].

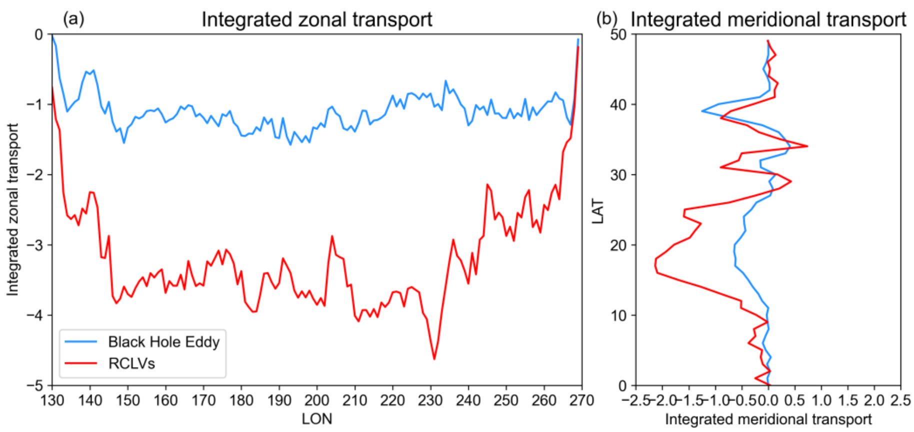

https://doi.org/10.5194/essd-2025-384
Preprint. Discussion started: 10 July 2025

Figure 19. (a) Meridionally integrated zonal transport (in Sv) and (b) zonally integrated meridional transport by BHEs (blue lines) and RCLVs (red lines).

3.7 Normalization and composite analysis with Chla, SST and SSS

Composite analysis in a rotated and normalized eddy coordinate system enables researchers to study the spatial patterns of eddy-related physical fields (Mcgillicuddy et al., 2007; Chelton et al., 2011a; Gaube et al., 2013; Delcroix et al., 2019; Trott et al., 2019; Yang et al., 2023; Wang et al., 2023). As suggested in Chen et al. (2021), oceanic eddies have a significant mean egg-like shape rather than a circle or ellipse considering the geophysical anisotropy in eddy properties. Consequently, following the methods used by and Chen et al. (2021), we computed normalized composite anomalies of Chla, SST, and SSS for BHEs in the North Pacific. The resulting composites are shown in normalized coordinates: Chla in Figure 20a and Figure 20b, SSTA in Figure 20c and Figure 20d, and SSS in Figure 20e and Figure 20f. The chla composites(Figure 20a and Figure 20b) reveal a clear monopole-like structure, with maximum anomalies concentrated at the eddy centers for both anticyclonic and cyclonic eddies. This centralized enhancement likely reflects the vertical transport of nutrients driven by Ekman pumping-upwelling in cyclonic eddies and downwelling in anticyclonic eddies-modulated by the eddies' asymmetric, egg-like geometry. The shape-imposed constraint not only affects physical transport but also strongly influences biological responses within the eddy cores (Fig. 18). Our findings are consistent with those of Chen et al. (2021), underscoring the role of eddy geometry in shaping ecosystem structure. Notably, SST and SSS anomalies exhibit spatial distributions similar to those of Chla anomalies, with centrally peaked patterns aligned with the eddy cores. This coherence across biophysical variables highlights the tight coupling between physical dynamics and biological responses within mesoscale eddies.

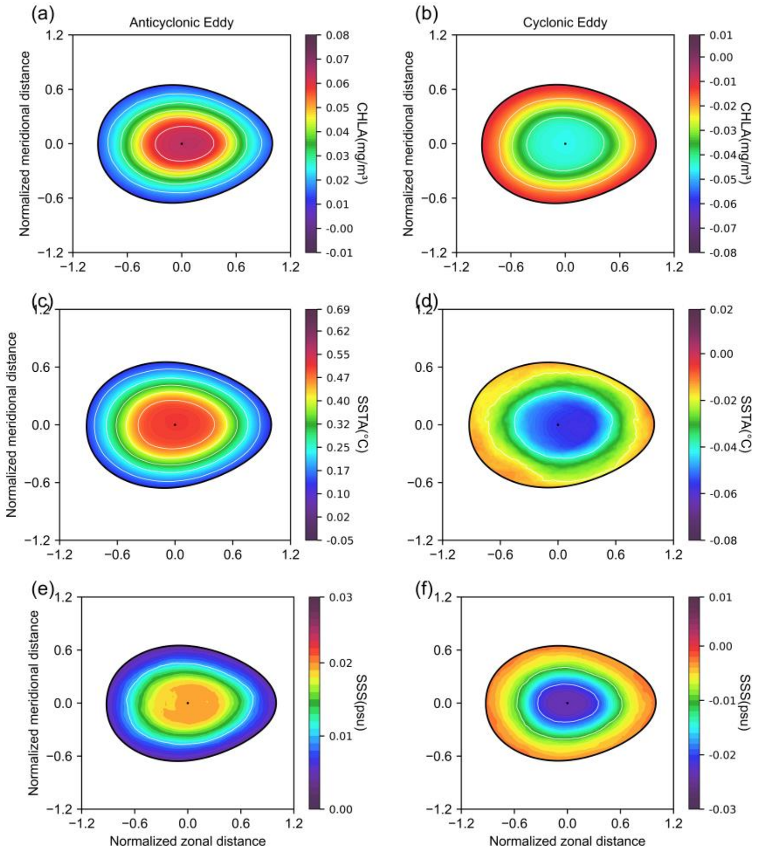

590

Figure 20. Normalized composite anomalies of chlorophyll *a* concentration (Chla), sea surface temperature (SST), and sea surface salinity (SSS) for anticyclonic (left column) and cyclonic (right column) BHEs in the North Pacific.

4 Dataset availability

The dataset BHE v1.0 can be accessed at https://doi.org/10.5281/zenodo.15597447 (Tian, F. L., Zhao, Y. Y., Long, S., and
595 Chen, G.: A Black Hole Eddy Dataset of North Pacific Ocean Based on Satellite Altimetry (BHE v1.0). Zenodo [data set], https://doi.org/10.5281/zenodo.15597447, 2025a. et al., 2025a). The identification dataset is saved in JSON format and the tracking dataset is saved in Pickle format. It is convenient to load the data using Python or other language. Detailed examples for using Python can be found in the data user manual, in which we also provide the related code to load and analyze BHE v1.0. Users can apply these algorithms to regional identification of BHE with different lifespans based on velocity fields
600 from observations or numerical simulations.

5 Conclusions

https://doi.org/10.5194/essd-2025-384
Preprint. Discussion started: 10 July 2025

In order to solve the problem of computational inefficiency caused by the high complexity and time-consuming Black Hole Eddy null-geodesic identification algorithm, we proposes an efficient Black Hole Eddy identification algorithm based on parallel acceleration of GPU, which realizes the efficient extraction of Black Hole Eddy. Through the comparative analysis, it is found that the efficiency of the GPU parallel acceleration algorithm is about 13 times higher than the original algorithm when calculating the BHE at a given day, enabling large-scale and long-time-span ocean data applications. Moreover, the tracking algorithm based on eddy-core advection is used to realize the construction of full-life trajectories of BHE.

Based on the efficient Black Hole Eddy identification algorithm and eddy-centered advction tracking algorithm, we constructed the a Black Hole Eddy dataset in the North Pacific Ocean for the years January 1, 1993 to May 5, 2023. The dataset includes the information of BHE with T=30 and 90 day respectively, and provides attributes including eddy boundaries, eddy types, eddy centers, radius, and stretching rates. Also, BHE v1.0 contains 18387 eddies with radius larger than 20 km and lifetimes longer than 4 weeks and captures the complete trajectories of BHE throughout their lifetimes. This is the first realization of the construction of a large-scale and long-time-span Black Hole Eddy identification and tracking dataset, which effectively fills a gap in the Black Hole Eddy dataset in oceanography.

Through comparisons of Lagrangian particle advection with Eulerian eddies and RCLVs, we demonstrate that Black Hole Eddy maintains strong material coherence and is able to maintain concentration during their life cycle. Unlike Eulerian eddies and RCLVs, which experience significant boundary deformation and mixing with the surrounding water during motion, BHE maintains a well-defined boundary and preserves their structure without significant filamentation or mixing with surrounding waters that effectively encloses and transports the water mass within. This remarkable material coherence underscores the importance of BHE in accurately estimating the transport capacity of oceanic features over extended periods. Furthermore, we found that almost 6% of BHEs do not overlap with any RCLVs or Eulerian eddies, which we term the Naked Black Hole Eddy that may be missed by Eulerian identification based on ADT and RCLVs identification entirely. Through the virtual Lagrangian particle advection validation and combined with ADT contour and LAVD contour, it is verified that the Naked Black Hole Eddy is characterized by strong coherence, which proved that the Naked Black Hole Eddy has a strong capability of wrapping the matter and its objectivity.

We compare the temporal and spatial distribution of BHEs with RCLVs. The spatial distribution of BHEs tends to be more in the mid-latitudes and less in the low-latitudes, and the number of RCLVs is much higher than that of BHEs, especially in the subtropical counter current and the California coastal current. In terms of temporal distribution, this study identifies similar interannual variations in BHEs occurrences with RCLVs. But RCLVs outnumber BHEs by about 5 times, which may imply that the RCLVs identification method is more likely to capture a larger number of long-lived eddies, whereas the BHE method may have a higher coherence requirement, resulting in a smaller number of eddies being identified. For BHEs, there are more anticyclonic eddies than cyclonic eddies, while the opposite is observed for RCLVs. Seasonal variations in the presentation of peaks in eddy frequency are observed in summer and lowest frequency occurring in January and February, with cyclonic BHEs being more prevalent than anticyclonic ones. These results suggest differing underlying dynamics governing the formation and persistence of these eddies, providing valuable insights into oceanic circulation patterns.

The statistical analysis highlights key differences between Black Hole Eddies and RCLVs. Black Hole Eddies exhibit a clear latitudinal dependence in size, with the mean radius decreasing beyond 40° latitude, reflecting the influence of geostrophic balance and Coriolis effects. At lower latitudes, Black Hole Eddies tend to have a larger and more dispersed radius, while at higher latitudes, their size becomes more constrained. In contrast, RCLVs show a relatively stable radius distribution without a clear monotonic trend. In terms of lifetime, both eddy types are predominantly concentrated within 4-6 weeks, with RCLVs showing a slightly higher probability density for shorter lifetimes. The peak radius for RCLVs is 51.39 km, slightly larger than the 44.52 km of Black Hole Eddies, but their overall distributions remain similar, with most eddies falling within the 30-70 km range. The joint probability density analysis further indicates that Black Hole Eddies are more concentrated in the small-coherent eddy category, while RCLVs tend to favor longer-lived and larger-radius eddies.

Regarding material transport, this study presents the zonal and meridional transport patterns of BHE, highlighting their consistent westward zonal transport in subtropical regions. It was found that the transport by BHEs are only about 1.5 Sv, which is lower than that of RCLVs about three times. BHEs exhibit more uniform transport patterns over time. This consistency in transport allows for more accurate assessments of material transport capacity compared to the overestimated values often associated with RCLVs. Additionally, we link BHE to biogeochemical processes, particularly in terms of Chla anomalies. Contrary to the dipolar structure observed in other eddy types, BHE exhibits a monopole-like structure, concentrating Chla within the eddy core. This finding emphasizes the significant role of BHE in influencing marine ecosystems and biogeochemical cycling.

With the continued advancement of satellite altimetry technology, future research can further expand the spatial and temporal scope of BHE datasets by incorporating more diverse and high-resolution data sources. In particular, integrating depth-resolved observations-such as those from Argo floats and ocean reanalysis data-such as the GLORYS12v1 dataset from CMEMS will enable a more detailed exploration of the three-dimensional structure and vertical dynamics of BHEs. Moreover, future studies may focus on the dynamic processes governing BHEs-such as their generation mechanisms and interactions with surrounding eddies or mesoscale features-providing new insights into their role in ocean circulation and mesoscale turbulence.

Video supplement. Video S1 (https://doi.org/10.5446/70890, Tian et al., 2025b): Comparison of the coherence between Eulerian Eddy, RCLVs and Black Hole Eddy, highlighting the coherence of Black Hole Eddy through the advection of Lagrangian particles. Video S2 (https://doi.org/10.5446/70891, Tian et al., 2025c): Analysis of the coherence of Naked Black Hole Eddy, highlighting the coherence of Naked Black Hole Eddy.

Author contributions. GC acquired funding and resources for the execution of the project. FT proposed the idea. FT, YZ and QL developed the related algorithm. FT and YZ organized the eddy dataset and conducted the data analysis. YZ, FT, SL wrote and edited the manuscript.

https://doi.org/10.5194/essd-2025-384
Preprint. Discussion started: 10 July 2025

Declaration of Generative AI in scientific writing. During the preparation of this work, the authors used WORDVICEAI in order to improve readability and language, not to replace key researcher tasks such as interpreting data or drawing scientific conclusions. After using this tool, the authors reviewed and edited the content as needed and took full responsibility for the content of the publication.

Competing interests. The contact author has declared that none of the authors has any competing interests.

Disclaimer. Publisher's note: Copernicus Publications remains neutral with regard to jurisdictional claims made in the text, published maps, institutional affiliations, or any other geographical representation in this paper. While Copernicus Publications makes every effort to include appropriate place names, the final responsibility lies with the authors.

Acknowledgment. We are very grateful to the anonymous Reviewers for the constructive comments and helpful suggestions which significantly help us to improve the quality of this paper. The altimeter data and the SSS data were freely downloaded from the CMEMS website (https://marine.copernicus.eu/). The high-resolution SST product was freely downloaded from the NOAA PSL website (https://psl.noaa.gov/data/gridded/data.noaa.oisst.v2.html). The mesoscale Eulerian eddy dataset was freely downloaded from the AVISO+ website at: https://data.aviso.altimetry.fr/aviso-gateway/data/META3.1exp_DT/.

Financial support. This work was jointly supported by National Natural Science Foundation of China (Grant No. 42030406) and the Science and Technology Innovation Project for Laoshan Laboratory (Grant Nos. LSKJ202201406 and LSKJ202204303).

References

Abernathey, R. and Haller, G.: Transport by Lagrangian Vortices in the Eastern Pacific, Journal of Physical Oceanography, 48, 667-685, https://doi.org/10.1175/JPO-D-17-0102.1, 2018.

Aurell, E., Boffetta, G., Crisanti, A., Paladin, G., and Vulpiani, A.: Predictability in the large: An extension of the concept of Lyapunov exponent, Journal of Physics a-Mathematical and General, 30, 1-26, https://doi.org/10.1088/0305-4470/30/1/003, 1997.

Beron-Vera, F. J., Olascoaga, M. J., Brown, M. G., and Koçak, H.: Zonal Jets as Meridional Transport Barriers in the Subtropical and Polar Lower Stratosphere, Journal of the Atmospheric Sciences, 69, 753-767, https://doi.org/10.1175/JAS-D-11-084.1, 2012.

Beron-Vera, F. J., Olascoaga, M. J., Brown, M. G., Koçak, H., and Rypina, II: Invariant-tori-like Lagrangian coherent structures in geophysical flows, Chaos, 20, https://doi.org/10.1063/1.3271342, 2010.

Beron-Vera, F. J., Wang, Y., Olascoaga, M. J., Goni, G. J., and Haller, G.: Objective Detection of Oceanic Eddies and the Agulhas Leakage, Journal of Physical Oceanography, 43, 1426-1438, https://doi.org/10.1175/JPO-D-12-0171.1, 2013.

Chaigneau, A., Gizolme, A., and Grados, C.: Mesoscale eddies off Peru in altimeter records: Identification algorithms and eddy spatio-temporal patterns, Progress in Oceanography, 79, 106-119, https://doi.org/10.1016/j.pocean.2008.10.013, 2008.

Chelton, D. B., Gaube, P., Schlax, M. G., Early, J. J., and Samelson, R. M.: The Influence of Nonlinear Mesoscale Eddies on Near-Surface Oceanic Chlorophyll, Science, 334, 328-332, https://doi.org/10.1126/science.1208897, 2011a.

Chelton, D. B., Schlax, M. G., and Samelson, R. M.: Global observations of nonlinear mesoscale eddies, Progress in Oceanography, 91, 167-216, https://doi.org/10.1016/j.pocean.2011.01.002, 2011b.

Chelton, D. B., Schlax, M. G., Samelson, R. M., and de Szoeke, R. A.: Global observations of large oceanic eddies, Geophysical Research Letters, 34, https://doi.org/10.1029/2007GL030812, 2007.

Chen, G., Yang, J., and Han, G. Y.: Eddy morphology: Egg-like shape, overall spinning, and oceanographic implications, Remote Sensing of Environment, 257, https://doi.org/10.1016/j.rse.2021.112348, 2021.

Chen, G. X., Gan, J. P., Xie, Q., Chu, X. Q., Wang, D. X., and Hou, Y. J.: Eddy heat and salt transports in the South China Sea and their seasonal modulations, Journal of Geophysical Research-Oceans, 117, https://doi.org/10.1029/2011JC007724, 2012.

d'Ovidio, F., Fernández, V., Hernández-García, E., and López, C.: Mixing structures in the Mediterranean Sea from finite-size Lyapunov exponents -: art. no. L17203, Geophysical Research Letters, 31, https://doi.org/10.1029/2004GL020328, 2004.

Delcroix, T., Chaigneau, A., Soviadan, D., Boutin, J., and Pegliasco, C.: Eddy-Induced Salinity Changes in the Tropical Pacific, Journal of Geophysical Research-Oceans, 124, 374-389, https://doi.org/10.1029/2018JC014394, 2019.

Dong, C. M., McWilliams, J. C., Liu, Y., and Chen, D. K.: Global heat and salt transports by eddy movement, Nature Communications, 5, https://doi.org/10.1038/ncomms4294, 2014.

Early, J. J., Samelson, R. M., and Chelton, D. B.: The Evolution and Propagation of Quasigeostrophic Ocean Eddies, Journal of Physical Oceanography, 41, 1535-1555, https://doi.org/10.1175/2011JPO4601.1, 2011.

Faghmous, J. H., Frenger, I., Yao, Y. S., Warmka, R., Lindell, A., and Kumar, V.: A daily global mesoscale ocean eddy dataset from satellite altimetry, Scientific Data, 2, https://doi.org/10.1038/sdata.2015.28, 2015.

Gaube, P., Chelton, D. B., Strutton, P. G., and Behrenfeld, M. J.: Satellite observations of chlorophyll, phytoplankton biomass, and Ekman pumping in nonlinear mesoscale eddies, Journal of Geophysical Research-Oceans, 118, 6349-6370, https://doi.org/10.1002/2013JC009027, 2013.

Haller, G.: A variational theory of hyperbolic Lagrangian Coherent Structures, Physica D-Nonlinear Phenomena, 240, 574-598, https://doi.org/10.1016/j.physd.2010.11.010, 2011.

Haller, G.: Lagrangian Coherent Structures, in: Annual Review of Fluid Mechanics, Vol 47, Annual Review of Fluid Mechanics, 137-162, https://doi.org/10.1146/annurev-fluid-010313-141322, 2015.

Haller, G. and Beron-Vera, F. J.: Geodesic theory of transport barriers in two-dimensional flows, Physica D-Nonlinear Phenomena, 241, 1680-1702, https://doi.org/10.1016/j.physd.2012.06.012, 2012.

Haller, G. and Beron-Vera, F. J.: Coherent Lagrangian vortices: the black holes of turbulence, Journal of Fluid Mechanics, 731, https://doi.org/10.1017/jfm.2013.391, 2013.

Haller, G., Hadjighasem, A., Farazmand, M., and Huhn, F.: Defining coherent vortices objectively from the vorticity, Journal of Fluid Mechanics, 795, 136-173, https://doi.org/10.1017/jfm.2016.151, 2016.

Haller, G., Karrasch, D., and Kogelbauer, F.: Material barriers to diffusive and stochastic transport, Proceedings of the National Academy of Sciences of the United States of America, 115, 9074-9079, https://doi.org/10.1073/pnas.1720177115, 2018.

He, Q., Tian, F. L., Yang, X. K., and Chen, G.: Lagrangian eddies in the Northwestern Pacific Ocean, Journal of Oceanology and Limnology, 40, 66-77, https://doi.org/10.1007/s00343-021-0392-7, 2022.

Henson, S. A. and Thomas, A. C.: A census of oceanic anticyclonic eddies in the Gulf of Alaska, Deep-Sea Research Part I-Oceanographic Research Papers, 55, 163-176, https://doi.org/10.1016/j.dsr.2007.11.005, 2008.

Jia, Y., Calil, P. H. R., Chassignet, E. P., Metzger, E. J., Potemra, J. T., Richards, K. J., and Wallcraft, A. J.: Generation of mesoscale eddies in the lee of the Hawaiian Islands, Journal of Geophysical Research-Oceans, 116, https://doi.org/10.1029/2011JC007305, 2011.

Jones-Kellett, A. E. and Follows, M. J.: A Lagrangian coherent eddy atlas for biogeochemical applications in the North Pacific Subtropical Gyre, Earth System Science Data, 16, 1475-1501, https://doi.org/10.5194/essd-16-1475-2024, 2024.

Joseph, B. and Legras, B.: Relation between kinematic boundaries, stirring, and barriers for the Antarctic polar vortex, Journal of the Atmospheric Sciences, 59, 1198-1212, https://doi.org/10.1175/1520-0469(2002)059<1198:RBKBSA>2.0.CO;2 , 2002.

Karrasch, D., Huhn, F., and Haller, G.: Automated detection of coherent Lagrangian vortices in two-dimensional unsteady flows, Proceedings of the Royal Society a-Mathematical Physical and Engineering Sciences, 471, https://doi.org/10.1098/rspa.2014.0639, 2015.

Karrasch, D. and Schilling, N.: Fast and robust computation of coherent Lagrangian vortices on very large two-dimensional domains %J The SMAI Journal of computational mathematics, 6, 101-124, https://doi.org/10.5802/smai-jcm.63, 2020.

Liu, T. Y. and Abernathey, R.: A global Lagrangian eddy dataset based on satellite altimetry, Earth System Science Data, 15, 1765-1778, https://doi.org/10.5194/essd-15-1765-2023, 2023.

Mason, E., Pascual, A., and McWilliams, J. C.: A New Sea Surface Height-Based Code for Oceanic Mesoscale Eddy Tracking, Journal of Atmospheric and Oceanic Technology, 31, 1181-1188, https://doi.org/10.1175/JTECH-D-14-00019.1, 2014.

McGillicuddy, D. J., Anderson, L. A., Bates, N. R., Bibby, T., Buesseler, K. O., Carlson, C. A., Davis, C. S., Ewart, C., Falkowski, P. G., Goldthwait, S. A., Hansell, D. A., Jenkins, W. J., Johnson, R., Kosnyrev, V. K., Ledwell, J. R., Li, Q. P., Siegel, D. A., and Steinberg, D. K.: Eddy/wind interactions stimulate extraordinary mid-ocean plankton blooms, Science, 316, 1021-1026, https://doi.org/10.1126/science.1136256, 2007.

Nencioli, F., Dong, C. M., Dickey, T., Washburn, L., and McWilliams, J. C.: A Vector Geometry-Based Eddy Detection Algorithm and Its Application to a High-Resolution Numerical Model Product and High-Frequency Radar Surface

Velocities in the Southern California Bight, Journal of Atmospheric and Oceanic Technology, 27, 564-579, https://doi.org/10.1175/2009JTECHO725.1, 2010.

Onu, K., Huhn, F., and Haller, G.: LCS Tool: A computational platform for Lagrangian coherent structures, Journal of Computational Science, 7, 26-36, https://doi.org/10.1016/j.jocs.2014.12.002, 2015.

Peacock, T. and Haller, G.: Lagrangian coherent structures The hidden skeleton of fluid flows, Physics Today, 66, 41-47, https://doi.org/10.1063/PT.3.1886, 2013.

Pegliasco, C., Delepoulle, A., Mason, E., Morrow, R., Faugère, Y., and Dibarboure, G.: META3.1exp: a new global mesoscale eddy trajectory atlas derived from altimetry, Earth System Science Data, 14, 1087-1107, https://doi.org/10.5194/essd-14-1087-2022, 2022.

Provenzale, A.: Transport by coherent barotropic vortices, Annual Review of Fluid Mechanics, 31, 55-93, https://doi.org/10.1146/annurev.fluid.31.1.55, 1999.

Qiu, B. and Chen, S. M.: Eddy-induced heat transport in the subtropical North Pacific from Argo, TMI, and altimetry measurements, Journal of Physical Oceanography, 35, 458-473, https://doi.org/10.1175/JPO2696.1, 2005.

Qiu, B., Chen, S. M., Klein, P., Sasaki, H., and Sasai, Y.: Seasonal Mesoscale and Submesoscale Eddy Variability along the North Pacific Subtropical Countercurrent, Journal of Physical Oceanography, 44, 3079-3098, https://doi.org/10.1175/JPO-D-14-0071.1, 2014.

Sadarjoen, I. A. and Post, F. H.: Detection, quantification, and tracking of vortices using streamline geometry, Computers & Graphics-Uk, 24, 333-341, https://doi.org/10.1016/S0097-8493(00)00029-7, 2000.

Serra, M. and Haller, G.: Objective Eulerian coherent structures, Chaos, 26, https://doi.org/10.1063/1.4951720, 2016.

Serra, M. and Haller, G.: Efficient computation of null geodesics with applications to coherent vortex detection, Proceedings of the Royal Society a-Mathematical Physical and Engineering Sciences, 473, https://doi.org/10.1098/rspa.2016.0807, 2017.

Shadden, S. C., Lekien, F., and Marsden, J. E.: Definition and properties of Lagrangian coherent structures from finite-time Lyapunov exponents in two-dimensional aperiodic flows, Physica D-Nonlinear Phenomena, 212, 271-304, https://doi.org/10.1016/j.physd.2005.10.007, 2005.

Tian, F. L., He, Q., Liu, Z. P., and Chen, G.: Extracting Lagrangian coherent structures in the Kuroshio current system, Ocean Dynamics, 69, 641-656, https://doi.org/10.1007/s10236-019-01262-6, 2019.

Tian, F. L., Wang, M. J., Liu, X., He, Q., and Chen, G.: SLA-Based Orthogonal Parallel Detection of Global Rotationally Coherent Lagrangian Vortices, Journal of Atmospheric and Oceanic Technology, 39, 823-836, https://doi.org/10.1175/JTECH-D-21-0103.1, 2022.

Tian, F. L., Wu, D., Yuan, L. M., and Chen, G.: Impacts of the efficiencies of identification and tracking algorithms on the statistical properties of global mesoscale eddies using merged altimeter data, International Journal of Remote Sensing, 41, 2835-2860, https://doi.org/10.1080/01431161.2019.1694724, 2020.

https://doi.org/10.5194/essd-2025-384
Preprint. Discussion started: 10 July 2025

Tian, F. L., Zhao, Y. Y., Long, S., and Chen, G.: A Black Hole Eddy Dataset of North Pacific Ocean Based on Satellite Altimetry (BHE v1.0). Zenodo [data set], https://doi.org/10.5281/zenodo.15597447, 2025a.

Tian, F. L., Zhao, Y. Y., Long, S., and Chen, G.: Comparison of the coherence between Eulerian Eddy, RCLVs and Black Hole Eddy, TIB AV-Portal [video], https://doi.org/10.5446/70890, 2025b.

Tian, F. L., Zhao, Y. Y., Long, S., and Chen, G.: Analysis of the coherence of Naked Black Hole Eddy, TIB AV-Portal [video], https://doi.org/10.5446/70891, 2025c.

Travis, S. and Qiu, B.: Decadal Variability in the South Pacific Subtropical Countercurrent and Regional Mesoscale Eddy Activity, Journal of Physical Oceanography, 47, 499-512, https://doi.org/10.1175/JPO-D-16-0217.1, 2017.

Trott, C. B., Subrahmanyam, B., Chaigneau, A., and Roman-Stork, H. L.: Eddy-Induced Temperature and Salinity Variability in the Arabian Sea, Geophysical Research Letters, 46, 2734-2742, https://doi.org/10.1029/2018GL081605, 2019.

Wang, H. L., Qiu, B., Liu, H. R., and Zhang, Z. G.: Doubling of surface oceanic meridional heat transport by non-symmetry of mesoscale eddies, Nature Communications, 14, https://doi.org/10.1038/s41467-023-41294-7, 2023.

Williams, S., Hecht, M., Petersen, M., Strelitz, R., Maltrud, M., Ahrens, J., Hlawitschka, M., and Hamann, B.: Visualization and Analysis of Eddies in a Global Ocean Simulation, Computer Graphics Forum, 30, 991-1000, https://doi.org/10.1111/j.1467-8659.2011.01948.x, 2011.

Wu, B. L. and Gan, J. P.: Seasonal Modulation of the Eddy Kinetic Energy and Subtropical Countercurrent Near the Western North Pacific Boundary, Journal of Geophysical Research-Oceans, 128, https://doi.org/10.1029/2022JC019160, 2023.

Xia, Q., Dong, C. M., He, Y. J., Li, G. C., and Dong, J. H.: Lagrangian Study of Several Long-Lived Agulhas Rings, Journal of Physical Oceanography, 52, 1049-1072, https://doi.org/10.1175/JPO-D-21-0079.1, 2022.

Yang, Y. K., Guo, Y. M., Zeng, L. L., and Wang, Q.: Eddy-induced sea surface salinity changes in the South China Sea, Frontiers in Marine Science, 10, https://doi.org/10.3389/fmars.2023.1113752, 2023.

Zhai, X. M., Greatbatch, R. J., and Kohlmann, J. D.: On the seasonal variability of eddy kinetic energy in the Gulf Stream region, Geophysical Research Letters, 35, https://doi.org/10.1029/2008GL036412, 2008.

Zhang, Z. G., Wang, W., and Qiu, B.: Oceanic mass transport by mesoscale eddies, Science, 345, 322-324, https://doi.org/10.1126/science.1252418, 2014.